

# Phonon-mediated spin dynamics in a two-electron double quantum dot under a phonon temperature gradient


Kazuyuki Kuroyama <sup>1,2,\*</sup>, Sadashige Matsuo <sup>2</sup>, Seigo Tarucha <sup>2,3,†</sup> and Yasuhiro Tokura <sup>4,‡</sup>

<sup>1</sup>*Institute of Industrial Science, The University of Tokyo, 7-3-1 Komaba, Meguro-ku, Tokyo, 153-8505, Japan*

<sup>2</sup>*Center for Emergent Materials Science (CEMS), RIKEN, 2-1 Hirosawa, Wako-shi, Saitama, 351-0198, Japan*

<sup>3</sup>*RIKEN Center for Quantum Computing (QCC), RIKEN, 2-1 Hirosawa, Wako-shi, Saitama, 351-0198, Japan*

<sup>4</sup>*Pure and Applied Sciences, University of Tsukuba, 1-1-1 Tennodai, Tsukuba, Ibaraki, 305-8571, Japan*

 (Received 9 March 2023; revised 14 August 2023; accepted 16 August 2023; published 20 September 2023)

We have theoretically studied phonon-mediated spin-flip processes of electrons in a GaAs double quantum dot (DQD) holding two spins, under a phonon temperature gradient over the DQD. Transition rates of interdot phonon-assisted tunnel processes and intradot spin-flip processes involving spin triplet states are formalized by the electron-phonon interaction accompanied with the spin-orbit interaction. The calculations of the spin-flip rates and the occupation probabilities of the spin-states in the two-electron DQD with respect to the phonon temperature difference between the dots are quantitatively consistent with our previous experiment. This theoretical study on the temperature gradient effect onto spins in coupled QDs would be essential for understanding spin-related thermodynamic physics.

DOI: [10.1103/PhysRevB.108.115308](https://doi.org/10.1103/PhysRevB.108.115308)

## I. INTRODUCTION

Thermodynamics in quantum mesoscopic systems has long been studied as one of the central concepts in solid-state physics. In particular, temperature gradients over mesoscopic structures have realized various kinds of thermodynamic functions such as heat engines and heat valves, which are useful for improvements of thermoelectric conversion and heat control by electrical means in mesoscopic devices [1–4], and there are many related theoretical studies that have been reported [5–11]. Although these kinds of thermodynamic phenomena are constituted mainly by a charge degree of freedom, when spin-related effects such as the spin-orbit interaction exist, contributions of the spin effects to thermodynamic phenomena cannot be dismissed. We have recently realized a lattice temperature gradient over a semiconductor double quantum dot (DQD) by using a nearby QD-based phonon source [12]. In this experimental study, we reveal that such a phonon source not only generates phonon-mediated spin transitions in the DQD, but also, due to the nonequilibrium phonon environment in the DQD, creates a significant imbalance in the occupation probabilities of parallel and antiparallel spin configurations in the two-electron DQD. This finding can provide intriguing concepts of spin-dependent thermoelectric devices that are driven by a local lattice temperature gradient. To date, many experimental and theoretical studies have been conducted on the phonon-mediated spin-dependent transitions in quantum dots to explore the dephasing mechanism of QD-based spin qubits [13–17], however, contributions of

a temperature gradient over coupled QDs to the transitions have never been discussed substantially. Therefore, theoretical studies on the temperature gradient effect would largely contribute to develop spin-related thermodynamic physics [1,18,19].

Based on this background, in this work, we have theoretically investigated the phonon-mediated spin-flip processes of two-electron spin states in a GaAs DQD under a phonon temperature gradient to reproduce our previous experiment [12]. Because spin-orbit interaction and electron-phonon interaction coexist in GaAs, a spin can flip during a phonon-mediated transition between ground states and excited states. Furthermore, we considered that the lattice temperatures are different between the two dots, i.e., there is a temperature gradient over the DQD. We successfully formalized the phonon-mediated spin-flip rates in such a nonequilibrium phonon environment. The ratio of the spin-flip tunnel rate from the right to left QD to that in the opposite direction shows clear dependence on the phonon temperature gradient between the QDs. Furthermore, we calculated the occupation probabilities of the two-electron spin states. The significant imbalance between antiparallel and parallel spin states found in our previous experiment is accurately reproduced by the theoretical calculation, which takes into account the nonequilibrium phonon environment in the DQD [12].

## II. TWO-ELECTRON SPIN STATES INVOLVING THE PHONON-MEDIATED PROCESSES

We considered the two-electron spin configurations of the  $(1, 1)$  and  $(0, 2)$  charge states in the DQD, where  $(i, j)$  denotes that the electron number  $i$  in the left QD and  $j$  in the right QD. It is assumed that the DQD is formed in a two-dimensional electron gas defined in a GaAs quantum

\*kuroyama@iis.u-tokyo.ac.jp

†Corresponding author: tarucha@riken.jp

‡tokura.yasuhiro.ft@u.tsukuba.ac.jp

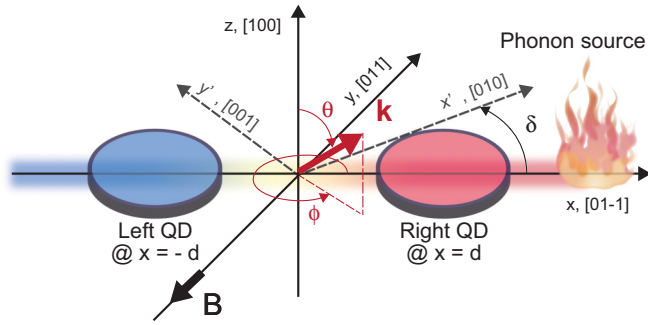


FIG. 1. Geometrical configuration of the DQD and the crystallographic orientations. The DQD array is aligned along the [01-1] crystallographic axis, which is denoted by  $x$ , and each dot is located at  $x = \pm d$ . The  $B$  field is applied in the [0-1-1] direction. The  $x'y'$  plane, that is spanned by [010] and [001] crystallographic axis, is used to express the spin-orbit interaction.

well [20]. The geometry of the DQD is depicted in Fig. 1. The spin states involving the phonon-mediated transition processes are summarized in Figs. 2(a) and 2(b). We assume that the two-electron DQD is set in the resonant condition of the (1, 1) and (0, 2) charge states, at which  $|\uparrow\downarrow(1, 1)\rangle$ ,  $|\downarrow\uparrow(1, 1)\rangle$ ,  $|T_+(1, 1)\rangle$ ,  $|T_-(1, 1)\rangle$ , and  $|S(0, 2)\rangle$  are energetically equivalent, and their energy differences

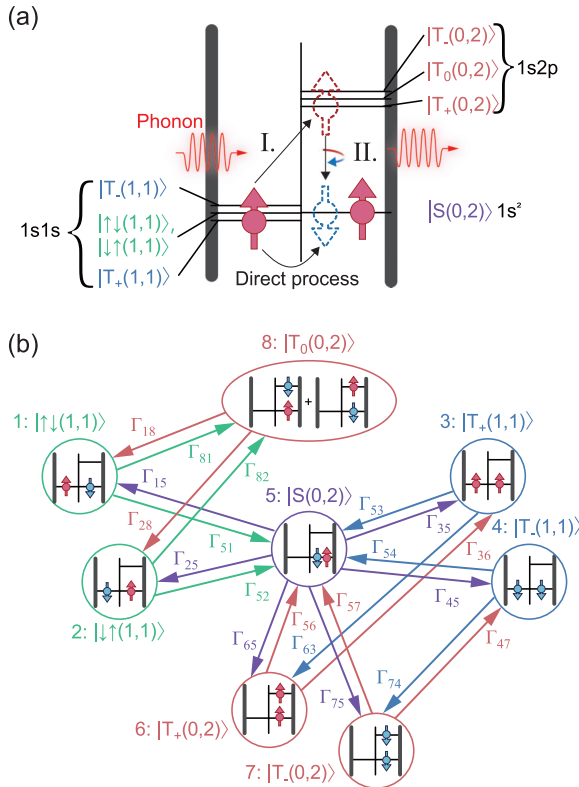


FIG. 2. (a) Energy diagram which explains the phonon-induced spin-flip tunnel processes in the two-electron DQD. A phonon excitation from  $|T_+(1, 1)\rangle$  to the excited state of  $|T_+(0, 2)\rangle$  (Process I), which is followed by the intradot spin-flip relaxation processes from  $|T_+(0, 2)\rangle$  to  $|S(0, 2)\rangle$  (Process II), is illustrated. (b) Transition diagram of the two-electron spin states with phonon excitations.

among the spin states of the (1, 1) charge state are negligible compared to the phonon thermal energy (see the detailed description in Appendix A). Here,  $T_\nu$ , where  $\nu = \pm$  and  $S$  denote the spin triplet and singlet states, respectively. Note that since we assume that the DQD is an isolated system, the electron number in the DQD is conserved. In addition, the (2, 0) charge state cannot be occupied because the energy is much higher than that of the (1, 1) and (0, 2) charge states in this setup. The excited states  $|T_\nu(0, 2)\rangle$  where  $\nu = 0, \pm$  are also taken into the consideration and are only accessed via the phonon excitation processes, that are discussed in detail in the next section [see also Fig. 2(a)]. We define  $|\Psi_i\rangle$  as the wave function of state  $i$  derived without the diagonalization of the two-electron Hamiltonian for the spin-orbit interaction (see Appendix A for the definition of  $|\Psi_i\rangle$ ). Thus,  $|\Psi_1\rangle, |\Psi_2\rangle = |\uparrow\downarrow(1, 1)\rangle, |\downarrow\uparrow(1, 1)\rangle$ , and  $|\Psi_3\rangle, |\Psi_4\rangle = |T_+(1, 1)\rangle, |T_-(1, 1)\rangle$ .  $|\Psi_5\rangle = |S(0, 2)\rangle$ , and  $|\Psi_6\rangle, |\Psi_7\rangle, |\Psi_8\rangle = |T_+(0, 2)\rangle, |T_-(0, 2)\rangle, |T_0(0, 2)\rangle$ .

### III. ELECTRON-PHONON INTERACTION

Next, we introduce the electron-phonon interaction. Figure 2(a) shows the energy diagram of the two-electron spin states in the DQD, which are involved in the phonon-mediated spin-flip tunnel processes. For the initial state,  $|T_+(1, 1)\rangle$ , the electron residing in the left QD can be excited to the  $2p$  orbital in the right QD, and the two electrons form  $|T_+(0, 2)\rangle$  [Process I in Fig. 2(a)]. Secondly, after this phonon-assisted interdot tunnel, the electron in the  $2p$  orbital rapidly relaxes to the  $1s$  orbital in the right QD to form  $|S(0, 2)\rangle$ , accompanied by the spin flip and the phonon emission [Process II in Fig. 2(a)]. Note that for  $|T_-(1, 1)\rangle$ , the same sequential phonon-mediated process to  $|S(0, 2)\rangle$  via  $|T_-(0, 2)\rangle$  takes place. Thus, this indirect spin-flip process between  $|T_\pm(1, 1)\rangle$  and  $|S(0, 2)\rangle$  via  $|T_\pm(0, 2)\rangle$  is added to the original direct spin-flip transitions between  $|T_\pm(1, 1)\rangle$  and  $|S(0, 2)\rangle$ , and therefore, the total spin-flip rates between  $|T_\pm(1, 1)\rangle$  and  $|S(0, 2)\rangle$  increase.

To estimate these phonon-mediated transition rates, we take into account the electron-phonon interaction. The Hamiltonian of the electron-phonon interaction is

$$\hat{\mathcal{H}}_{e-p} = \sum_{\mu, \mathbf{k}} \sum_{ij} \Lambda_{\mu, \mathbf{k}, ij} |\xi_i\rangle \langle \xi_j| (\hat{b}_{\mu, \mathbf{k}}^\dagger + \hat{b}_{\mu, -\mathbf{k}}), \quad (1)$$

where  $\mu$  and  $\mathbf{k}$  represent the mode and the wave number of a phonon, respectively, and  $\hat{b}_{\mu, \mathbf{k}}$  and  $\hat{b}_{\mu, \mathbf{k}}^\dagger$  are the corresponding annihilation and creation operators satisfying the commutation relation:  $[\hat{b}_{\mu, \mathbf{k}}, \hat{b}_{\mu', \mathbf{k}'}^\dagger] = \delta_{\mu, \mu'} \delta_{\mathbf{k}, \mathbf{k}'}$ .  $\Lambda_{\mu, \mathbf{k}, ij} \equiv \lambda_{\mu, \mathbf{k}} \langle \xi_i | e^{i\mathbf{k} \cdot \mathbf{r}_1} + e^{i\mathbf{k} \cdot \mathbf{r}_2} | \xi_j \rangle$ .  $\mathbf{r}_i$  represents the position of the  $i$ th electron, and  $\lambda_{\mu, \mathbf{k}}$  is the electron-phonon coupling parameter.  $|\xi_i\rangle$  is the eigenstates of the two-electron spin wave functions and in an orthonormal basis for the first-order perturbation theory for the spin-orbit interaction (see Appendix A for a description of how to derive  $|\xi_i\rangle$  from  $|\Psi_i\rangle$ ). Hence, please note that  $|\xi_1\rangle, |\xi_2\rangle \simeq |\uparrow\downarrow(1, 1)\rangle, |\downarrow\uparrow(1, 1)\rangle$ , and  $|\xi_3\rangle, |\xi_4\rangle \simeq |T_+(1, 1)\rangle, |T_-(1, 1)\rangle$ .  $|\xi_5\rangle \simeq |S(0, 2)\rangle$ , and  $|\xi_6\rangle, |\xi_7\rangle, |\xi_8\rangle \simeq |T_+(0, 2)\rangle, |T_-(0, 2)\rangle, |T_0(0, 2)\rangle$ . In addition, we note that  $|\xi_i\rangle$  is used only for the phonon-induced transitions, in order to take into account the simultaneous action of the spin-orbit interaction and the electron-phonon interaction, and the other

TABLE I. Summary of the definitions for the wave functions used in the paper.

Single electron wave functions from the Fock-Darwin states	$\psi_i$ ( $i = L, R, R^*$ )
Single electron wave functions orthogonalized for the interdot overlap	$\tilde{\psi}_i$ ( $i = L, R, R^*$ )
Spin wave functions of two electrons	$\chi_i$ ( $i = S, T0, T\pm$ )
Two-electron wave functions constituted by $\tilde{\psi}_i$ and $\chi_i$	$\Psi_i$ ( $i = 1, \dots, 8$ )
Orthogonalized Two-electron wave functions for the spin-orbit interaction	$\xi_i$ ( $i = 1, \dots, 8$ )

transitions taking place in the ground states are calculated by  $|\Psi_i\rangle$  (see also Table I for the descriptions of the wave functions used in the paper). Based on the Fermi's golden rule, the transition rate from level  $n$  to level  $m$  via absorption or emission of one phonon is

$$\gamma_{mn} \equiv \frac{2\pi}{\hbar} \sum_{\mu, \mathbf{k}} |\Lambda_{\mu, \mathbf{k}, mn}|^2 [n_{\mu, \mathbf{k}}^a \delta(\epsilon_n - \epsilon_m + \hbar\omega_{\mu, \mathbf{k}}) + (n_{\mu, \mathbf{k}}^a + 1) \delta(\epsilon_n - \epsilon_m - \hbar\omega_{\mu, \mathbf{k}})], \quad (2)$$

where  $n_{\mu, \mathbf{k}}^a$  is the phonon distribution function contributing to the processes  $a = |\xi_3\rangle \leftrightarrow |\xi_6\rangle$  and  $|\xi_4\rangle \leftrightarrow |\xi_7\rangle$  ( $\sim |T_{\pm}(1, 1)\rangle \leftrightarrow |T_{\pm}(0, 2)\rangle$ ) and  $a = |\xi_5\rangle \leftrightarrow |\xi_6\rangle$  and  $|\xi_5\rangle \leftrightarrow |\xi_7\rangle$  ( $\sim |S(0, 2)\rangle \leftrightarrow |T_{\pm}(0, 2)\rangle$ ). In the global equilibrium condition, based on spatial uniformity,  $n_{\mu, \mathbf{k}}(T) \equiv 1/(e^{\hbar\omega_{\mu, \mathbf{k}}/(k_B T)} - 1)$ , where  $k \equiv |\mathbf{k}|$ . Here, to consider the phonon temperature gradient over the DQD, we introduce individual phonon temperatures  $T_L$  for the transition  $|\xi_3\rangle \leftrightarrow |\xi_6\rangle$  (and  $|\xi_4\rangle \leftrightarrow |\xi_7\rangle$ ), and  $T_R$  for the transition  $|\xi_5\rangle \leftrightarrow |\xi_6\rangle$  (and  $|\xi_5\rangle \leftrightarrow |\xi_7\rangle$ ). The transition rates between states  $|\xi_5\rangle$  and  $|\xi_6\rangle$ , and those between states  $|\xi_3\rangle$  and  $|\xi_6\rangle$  are described by using the phonon temperatures:

$$\Gamma_{56} = \gamma_0(1 + n_{\mu, k_{\Delta}}(T_R)), \quad (3)$$

$$\Gamma_{65} = \gamma_0 n_{\mu, k_{\Delta}}(T_R), \quad (4)$$

$$\Gamma_{36} = \gamma'_0(1 + n_{\mu, k_{\Delta}}(T_L)), \quad (5)$$

$$\Gamma_{63} = \gamma'_0 n_{\mu, k_{\Delta}}(T_L), \quad (6)$$

where  $\Delta$  is the energy separation between  $|S(0, 2)\rangle$  and  $|T_0(0, 2)\rangle$  (see Appendix A), and  $k_{\Delta} \equiv \Delta/(\hbar c_{\mu})$ .  $\Gamma_{ij}$  denotes the transition rate from state  $j$  to  $i$ . The coefficients,  $\gamma_0$  and  $\gamma'_0$ , in Eqs. (3) and (5) are derived by the following calculations:

$$\begin{aligned} \gamma_0 &\equiv \frac{2\pi}{\hbar} \sum_{\mu, \mathbf{k}} |\Lambda_{\mu, \mathbf{k}, 56}|^2 \delta(\Delta - \hbar\omega_{\mu, \mathbf{k}}) \\ &\simeq \frac{2\pi}{\hbar} \sum_{\mu} \langle |\Lambda_{\mu, \mathbf{k}, 56}|^2 \rangle_{k_{\Delta}} v_{\mu}(k_{\Delta}), \end{aligned} \quad (7)$$

$$\begin{aligned} \gamma'_0 &\equiv \frac{2\pi}{\hbar} \sum_{\mu, \mathbf{k}} |\Lambda_{\mu, \mathbf{k}, 36}|^2 \delta(\Delta - \hbar\omega_{\mu, \mathbf{k}}) \\ &\simeq \frac{2\pi}{\hbar} \sum_{\mu} \langle |\Lambda_{\mu, \mathbf{k}, 36}|^2 \rangle_{k_{\Delta}} v_{\mu}(k_{\Delta}), \end{aligned} \quad (8)$$

where  $v_{\mu}(k) \equiv V k^2 / (2\pi^2 \hbar c_{\mu})$  and  $c_{\mu}$  are the phonon density of states of mode  $\mu$  and a sound velocity of  $\mu$ , respectively.  $\mu$  denotes either a longitudinal acoustic phonon ( $\mu = l$ ) or a transverse acoustic phonon ( $\mu = t$ ).  $V = L^3$  is the system volume. The square of the phonon matrix element,  $\langle |\Lambda_{\mu, \mathbf{k}, ij}|^2 \rangle_{k_{\Delta}}$ , is approximated by its average value over the surface of the wave number space defined as  $|\mathbf{k}| = k_{\Delta}$ :

$$\langle |\Lambda_{\mu, \mathbf{k}, ij}|^2 \rangle_{k_{\Delta}} \equiv \frac{1}{4\pi} \int_0^{2\pi} d\phi \int_0^{\pi} d\theta \sin\theta |\Lambda_{\mu, \mathbf{k}, ij}|^2_{|\mathbf{k}|=k_{\Delta}}, \quad (9)$$

where the orientation of the wave number,  $\mathbf{k}/k = (\sin\theta \cos\phi, \sin\theta \sin\phi, \cos\theta)$ , is represented by the spherical coordinate (see a red arrow in Fig. 1 for the definition of  $\mathbf{k}$ ).

For the derivation of the phonon matrix elements  $\Lambda_{\mu, \mathbf{k}, ij}$ , we calculate the bracket product of  $\langle \xi_i | e^{i\mathbf{k}\cdot\mathbf{r}} | \xi_j \rangle$  based on the wave functions perturbed by the spin-orbit interaction. Phonons do not alter the electron spin states and solely interact with electrons individually; therefore, the nonzero matrix elements of  $\hat{O}_{\mathbf{k}} \equiv \sum_{i=1,2} e^{i\mathbf{k}\cdot\mathbf{r}_i}$ , i.e., the main part of the electron-phonon interaction Hamiltonian, is

$$\langle \xi_n | \hat{O}_{\mathbf{k}} | \xi_m \rangle = \sum_{j=1, j'=1}^8 C_{nj}^* C_{mj'} \langle \Psi_j | \hat{O}_{\mathbf{k}} | \Psi_{j'} \rangle. \quad (10)$$

At the weak coupling regime of a DQD, the off-diagonal components can be neglected because they are much smaller by a factor of  $e^{-d^2/l_0^2}$  than the diagonal components, where  $d$  is half the distance between the two dots (see Fig. 1) and  $l_0$  is the confinement length of an electron in the QD. Therefore, using only the diagonal components, we can express the matrix elements explicitly as

$$\begin{aligned} \langle \xi_n | \hat{O}_{\mathbf{k}} | \xi_m \rangle &\simeq \sum_{j=1}^8 C_{nj}^* C_{mj} O_R + \sum_{j=1}^4 C_{nj}^* C_{mj} O_L \\ &\quad + C_{n5}^* C_{m5} O_R + \sum_{j=6}^8 C_{nj}^* C_{mj} O_{R^*}, \end{aligned} \quad (11)$$

where  $O_L \equiv \langle \tilde{\psi}_L | e^{i\mathbf{k}\cdot\mathbf{r}} | \tilde{\psi}_L \rangle$ ,  $O_R \equiv \langle \tilde{\psi}_R | e^{i\mathbf{k}\cdot\mathbf{r}} | \tilde{\psi}_R \rangle$  and  $O_{R^*} \equiv \langle \tilde{\psi}_{R^*} | e^{i\mathbf{k}\cdot\mathbf{r}} | \tilde{\psi}_{R^*} \rangle$  (see Appendix B for the definitions of a single electron wave functions in the DQD,  $\tilde{\psi}_L$ ,  $\tilde{\psi}_R$ , and  $\tilde{\psi}_{R^*}$ ). Based on the above results, the off-diagonal element between state  $|\xi_6\rangle$  ( $\simeq |T_+(0, 2)\rangle$ ) and  $|\xi_5\rangle$  ( $\simeq |S(0, 2)\rangle$ ) is

$$\begin{aligned} \langle \xi_6 | \hat{O}_{\mathbf{k}} | \xi_5 \rangle &\simeq \frac{\alpha \tau_{LR^*}}{\Delta E_Z} (O_L + O_R) + \frac{\beta}{\Delta + E_Z} (O_R - O_{R^*}) \\ &\simeq \frac{\alpha \tau_{LR^*}}{\Delta E_Z} (O_L + O_R) + \frac{\beta}{\Delta} (O_R - O_{R^*}), \end{aligned} \quad (12)$$

where it is assumed that Zeeman energy of a single electron spin,  $E_Z$ , satisfies that  $E_Z \ll \Delta$  from our previous experimental condition of  $B = 0.1$  T [12].  $\tau_{LR^*}$  is the tunnel coupling between the ground state in the left QD and the first-excited state in the right QD (see Appendix B for the definition of  $\tau_{LR^*}$ ).  $\alpha$  is the spin-orbit coupling between states 3 or 4 and 5, and  $\beta$  is that between states 5 and 6 or 7 (see Appendix A for the definitions of  $\alpha$  and  $\beta$ ). For the weak interdot coupling condition, since  $\alpha$  is much smaller than  $E_Z$ , the first term in

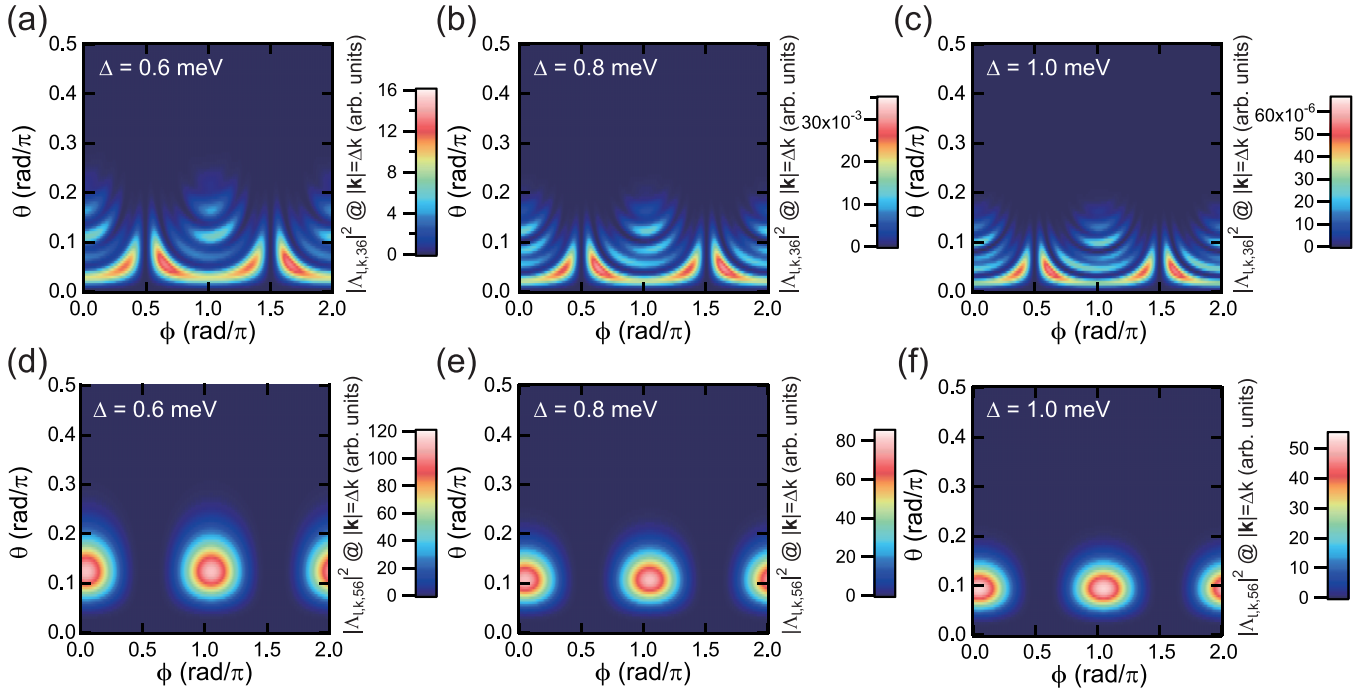


FIG. 3. [(a)–(c)] Color-coded maps of  $|\Delta_{l,k,36}|^2$  calculated for the different  $\mathbf{k}$ -vector orientations,  $\theta$  and  $\phi$ , at  $\Delta = 0.6, 0.8,$  and  $1.0$  meV, respectively. Phonons propagating in the angle marked in a bright color contribute to the electron-phonon interaction. Note that since the electron-phonon interaction is symmetric with respect to  $z = 0$ , the color-coded maps are plotted only for  $0 \leq \theta \leq 0.5\pi$ . [(d)–(f)] Color-coded maps of  $|\Delta_{\mu,k,56}|^2$  calculated for the different  $\mathbf{k}$ -vector orientations, at  $\Delta = 0.6, 0.8,$  and  $1.0$  meV, respectively.

Eq. (12) can be ignored as

$$\langle \xi_6 | \hat{O}_{\mathbf{k}} | \xi_5 \rangle \simeq \frac{\beta}{\Delta} (O_R - O_{R^*}). \quad (13)$$

Similarly, the off-diagonal element between states  $|\xi_6\rangle$  ( $\simeq |T_+(0, 2)\rangle$ ) and  $|\xi_3\rangle$  ( $\simeq |T_+(1, 1)\rangle$ ) is

$$\langle \xi_3 | \hat{O}_{\mathbf{k}} | \xi_6 \rangle \simeq -\frac{\tau_{LR}^*}{\Delta} (O_L - O_{R^*}). \quad (14)$$

Regarding the  $T_-$  states, the off-diagonal elements between states  $|\xi_7\rangle$  ( $\simeq |T_-(0, 2)\rangle$ ) and  $|\xi_5\rangle$  ( $\simeq |S(0, 2)\rangle$ ) and between states  $|\xi_4\rangle$  ( $\simeq |T_-(1, 1)\rangle$ ) and  $|\xi_7\rangle$  ( $\simeq |T_-(0, 2)\rangle$ ) can also be determined:

$$\langle \xi_7 | \hat{O}_{\mathbf{k}} | \xi_5 \rangle \simeq \frac{\beta}{\Delta} (O_R - O_{R^*}), \quad (15)$$

$$\langle \xi_4 | \hat{O}_{\mathbf{k}} | \xi_7 \rangle \simeq -\frac{\tau_{LR}^*}{\Delta} (O_L - O_{R^*}). \quad (16)$$

Similarly, regarding the  $T_0$  state, the off-diagonal elements between states  $|\xi_1\rangle$  and  $|\xi_8\rangle$  and between states  $|\xi_2\rangle$  and  $|\xi_8\rangle$  are described as  $\langle \xi_1 | \hat{O}_{\mathbf{k}} | \xi_8 \rangle \simeq -\langle \xi_2 | \hat{O}_{\mathbf{k}} | \xi_8 \rangle \simeq -\tau_{LR}^* (O_L - O_{R^*}) / (\sqrt{2}\Delta)$ . Note that since the spin wave functions of states 5 and 8 are orthogonal and the electron-phonon interaction cannot alter the spin state of electrons in the QD, the transition between the two states is not allowed. In addition, even if the spin-orbit interaction accompanies the electron-phonon interaction, their simultaneous action changes the spin state from  $|S(0, 2)\rangle$  to either  $|T_+(0, 2)\rangle$  or  $|T_-(0, 2)\rangle$  and allows only the transitions between states 5 and 6 and between states 5 and 7, as discussed above. Therefore, in our model, transitions between states 5 and 8 never take place.

Next, we introduce the electron-phonon coupling coefficient  $\lambda_{\mu,k}$ , into the calculation of  $\Delta_{\mu,k,ij}$ . The possible contributions in GaAs QDs are related to the piezo-electric effect and the deformation potential. We confirmed that, for a phonon energy around  $\Delta \sim 1$  meV, the electron-phonon coupling is dominated by the deformation potential [16], and the piezoelectric effect can be neglected [17]. Therefore, we only considered the deformation potential. The electron-phonon coupling coefficient of the deformation potential is described by  $\lambda_{\mu=l,k} = \sqrt{\hbar/(2V\rho c_l)}(-i\sqrt{|\mathbf{k}|}\Xi)$ , where  $\rho$  is the mass density of GaAs, and  $c_l$  is the velocity of a longitudinal acoustic phonon.  $\Xi$  is the deformation potential of GaAs. In the following calculations, only longitudinal acoustic phonons ( $\mu = l$ ) with the energy  $\Delta$  are considered.

#### IV. EVALUATION OF THE PHONON-MEDIATED SPIN-FLIP TUNNEL RATES

We calculated  $|\Delta_{l,k,36}|^2$  at  $|\mathbf{k}| = k_\Delta$ . The color-coded maps of  $|\Delta_{l,k,36}|^2$  as functions of  $\theta$  and  $\phi$  for the  $|S(0, 2)\rangle$ – $|T_0(0, 2)\rangle$  energy separation  $\Delta = 0.6, 0.8,$  and  $1.0$  meV are shown in Figs. 3(a), 3(b) and 3(c), respectively. The physical constants and parameters used in the calculations are listed in Table II. Note that because of the symmetry of the DQD system with respect to  $z = 0$ , we only plot in the range of  $0 \leq \theta \leq 0.5\pi$ . The half interdot distance  $d$  is set to be 96 nm. According to the color-coded maps, the electron-phonon coupling strength enhances only in  $0 < \theta < 0.2\pi$ . This indicates that, for  $\Delta$  in this energy range, only phonons which propagate mostly perpendicularly to the  $xy$  plane can interact with the electrons in the DQD. As confirmed by the definition of the electron-phonon coupling [see Eqs. (7) and (8)], only phonons

TABLE II. Values of the constants used in the calculations.

Mass density of GaAs, $\rho$	5300 kg/m <sup>3</sup>
Speed of sound for longitudinal phonons in GaAs, $c_l$	4700 m/s
Deformation potential of GaAs, $\Xi$ [17]	13.7 eV
Electron Lande $g$ factor	-0.44
Quantum well length, $l_z$	15 nm
Magnetic field, $B$	0.1 T
Spin-orbit length, $\lambda_{so}$ [21–23]	1 $\mu$ m

whose energy is in resonance with  $\Delta$  contribute to the electron-phonon coupling. In addition, the electron-phonon coupling is maximized when the dimension of the in-plane component of the phonon wave number vector along the quantum well surface matches the lateral dimension of the electron wave functions in the DQD. These two requirements are simultaneously satisfied when  $\theta \sim 0.1\pi$ . Furthermore, in these color-coded maps, more complicated structures originated from the interdot distance  $d$  appear. The color-coded maps of  $|\Lambda_{l,k,56}|^2$  calculated for the same values of  $\Delta$  as  $|\Lambda_{l,k,36}|^2$ , are shown in Figs. 3(d), 3(e) and 3(f). Since the wave function of the excited state in the right QD,  $\tilde{\psi}_{R^*}$ , is expanded mostly along the  $x$  axis (see Appendix B for the definition of  $\tilde{\psi}_{R^*}$ ), the larger electron-phonon coupling shows up at around  $\phi = 0$  and  $\pi$ .

We computed the spin-conserving tunnel rate  $\Gamma_{15}$  and the spin-flip tunnel rate  $\Gamma_{35}$  for the ground states as functions of  $\Delta$  and  $d$ . Note that we assume that the time scale of the interdot tunneling events is much larger than the coherence time of the orbitals of electrons in the QD. In the weak coupling regime, these rates are defined by using Fermi's golden rule [24–26]:

$$\begin{aligned}\Gamma_{15}(\epsilon) &= \frac{2\pi}{\hbar} |\langle \Psi_1 | \hat{H}_{\text{QD},2e} | \Psi_5 \rangle|^2 P(\epsilon) \\ &= \frac{2\pi}{\hbar} |\tau_{LR}|^2 P(\epsilon),\end{aligned}\quad (17)$$

where  $\hat{H}_{\text{QD},2e}$  is the Hamiltonian of the two electrons in the DQD without the electron-phonon interaction (see Appendix A for the definition).  $\tau_{LR}$  is the tunnel coupling between the ground states in the DQD (see Appendix B for the definition).  $\epsilon$  and  $P(\epsilon)$  are the energy detuning between states 1 and 5 and the probability that the electrons exchange energy  $\epsilon$  with the surrounding environment, respectively [24].  $P(\epsilon)$  represents the broadening of the interdot tunnel rate spectrum, for example by the time independent fluctuation of the QD energy level induced by the gate voltage instability [26]. We do not discuss the mechanism of  $P(\epsilon)$ , but from previous experimental studies, it can be assumed that  $\Gamma_{15}(\epsilon) = \Gamma_{15} \exp(-\epsilon^2/2\delta_\epsilon^2)$ , where  $\delta_\epsilon$  represents the linewidth of the interdot tunnel rate spectrum. Thereby, by integrating both sides of Eq. (17) by  $\epsilon$ , the incoherent tunnel rates under the resonance condition, i.e., for  $\epsilon = 0$ , can be described as

$$\Gamma_{15} = \frac{\sqrt{2\pi} |\tau_{LR}|^2}{\hbar \delta_\epsilon}.\quad (18)$$

In the calculations, we adopted  $\delta_\epsilon \sim 100 \mu\text{eV}$  estimated from our previous experiment [12]. Similarly, the spin-flip tunnel rates between the ground states of the left and right QDs,  $\Gamma_{35}$ ,

is

$$\Gamma_{35} = \frac{\sqrt{2\pi} |\alpha|^2}{\hbar \delta_\epsilon}.\quad (19)$$

Figures 4(a) and 4(b) show the calculated values of  $\Gamma_{15}$  and  $\Gamma_{35}$  plotted as functions of  $\Delta$  and  $d$ . Both rates show a very similar dependence in the plane of  $\Delta$  and  $d$ , meaning that the spin-flip tunnel rate of the ground states is proportional to the spin-conserving tunnel rate. This behavior is consistent with previous experimental and theoretical studies [17,23,27]. Next, we calculated the transition rates,  $\gamma_0$  and  $\gamma'_0$ , for various values of  $\Delta$  and  $d$ . Figure 4(c) shows  $\gamma_0$  plotted for the different  $\Delta$ . Note that since  $\gamma_0$  is the transition rate of the intradot spin-flip process, it is independent of the interdot distance  $d$ .  $\gamma_0$  stays at around 400 kHz for  $0.4 \leq \Delta \leq 1 \text{ meV}$  [13–15,28].  $\gamma'_0$  calculated for various values of  $\Delta$  and  $d$  is shown in the color-coded map of Fig. 4(d).  $\gamma'_0$  varies over a much wider range than  $\gamma_0$ . The dependence on  $d$  is understood by the fact that the interdot tunnel coupling energy increases as  $d$  decreases. Furthermore, the  $\Delta$  dependence of  $\gamma'_0$  is also explained by the interdot tunnel coupling, because  $l_0$  decreases as  $\Delta$  increases [see Eq. (B15)] in Appendix B, and  $e^{-d^2/l_0^2}$  in  $\tau_{LR}$  decreases accordingly. We chose  $\Delta = 0.8 \text{ meV}$  and  $d = 100 \text{ nm}$  for the following calculations, in such a way that  $\Gamma_{15}$  is on the orders of a few kHz, and  $\Gamma_{35}$  is below a few Hz as obtained in our previous experimental study. For those values of  $\Delta$  and  $d$ ,  $\Gamma_{15} \sim 2.2 \text{ kHz}$ ,  $\Gamma_{35} \sim 0.47 \text{ Hz}$ ,  $\gamma_0 \sim 410 \text{ kHz}$ , and  $\gamma'_0 \sim 170 \text{ Hz}$  are calculated.

Next, we calculated the phonon-mediated spin-flip tunnel rates in the DQD when the phonon temperatures in the left and right QDs, i.e.,  $T_L$  and  $T_R$ , are different. If  $\gamma_0 \gg \gamma'_0$ , we can describe the spin-flip tunnel rate from the left to right QD,  $\Gamma_{R \leftarrow L}$ , as follows [12] [see Fig. 2(b) and Appendix D].

$$\begin{aligned}\Gamma_{R \leftarrow L} &\simeq \Gamma_{53} + \Gamma_{63} \\ &= \Gamma_{53} + \gamma'_0 n_{l,k_\Delta}(T_L).\end{aligned}\quad (20)$$

For the opposite tunneling direction, by considering the occupation probabilities of the spin states of (0, 2) for a case that the intradot phonon excitation rates ( $\Gamma_{65}$ ,  $\Gamma_{75}$ ) and the intradot phonon relaxation rates ( $\Gamma_{56}$ ,  $\Gamma_{57}$ ) are much faster than the other transition rates, we describe the spin-flip tunnel rate from the right to left QD,  $\Gamma_{L \leftarrow R}$  as

$$\begin{aligned}\Gamma_{L \leftarrow R} &\simeq \frac{\Gamma_{56}}{\Gamma_{65} + \Gamma_{56}} (\Gamma_{35} + \Gamma_{45}) + \frac{2\Gamma_{65}}{2\Gamma_{65} + \Gamma_{56}} \Gamma_{36} \\ &= 2 \frac{n_{l,k_\Delta}(T_R) + 1}{3n_{l,k_\Delta}(T_R) + 1} \Gamma_{35} + \frac{2n_{l,k_\Delta}(T_R)}{3n_{l,k_\Delta}(T_R) + 1} \\ &\quad \times \gamma'_0 [1 + n_{l,k_\Delta}(T_L)],\end{aligned}\quad (21)$$

where  $\Gamma_{56}/(2\Gamma_{65} + \Gamma_{56})$  represents the occupation probability of either state 6 or 7, and  $2\Gamma_{65}/(2\Gamma_{65} + \Gamma_{56})$  does that of state 5 in the (0, 2) charge state. We assume that the Zeeman energy induced by the  $B$  field is sufficiently small compared to a thermal energy of electrons in the DQD, so that states 3 and 4, and states 6 and 7 are nearly degenerated, i.e.,  $\Gamma_{35} \simeq \Gamma_{45}$ ,  $\Gamma_{53} \simeq \Gamma_{54}$ ,  $\Gamma_{65} \simeq \Gamma_{75}$ , and  $\Gamma_{56} \simeq \Gamma_{57}$ . We plot  $\Gamma_{R \leftarrow L}$  with respect to  $T_L$  in Fig. 5(a), where  $d = 96 \text{ nm}$  and  $\Delta = 0.8 \text{ meV}$ . When  $T_L > 2 \text{ K}$ , since the population of phonons with the energy  $\Delta$  starts to increase, the phonon-mediated interdot transitions

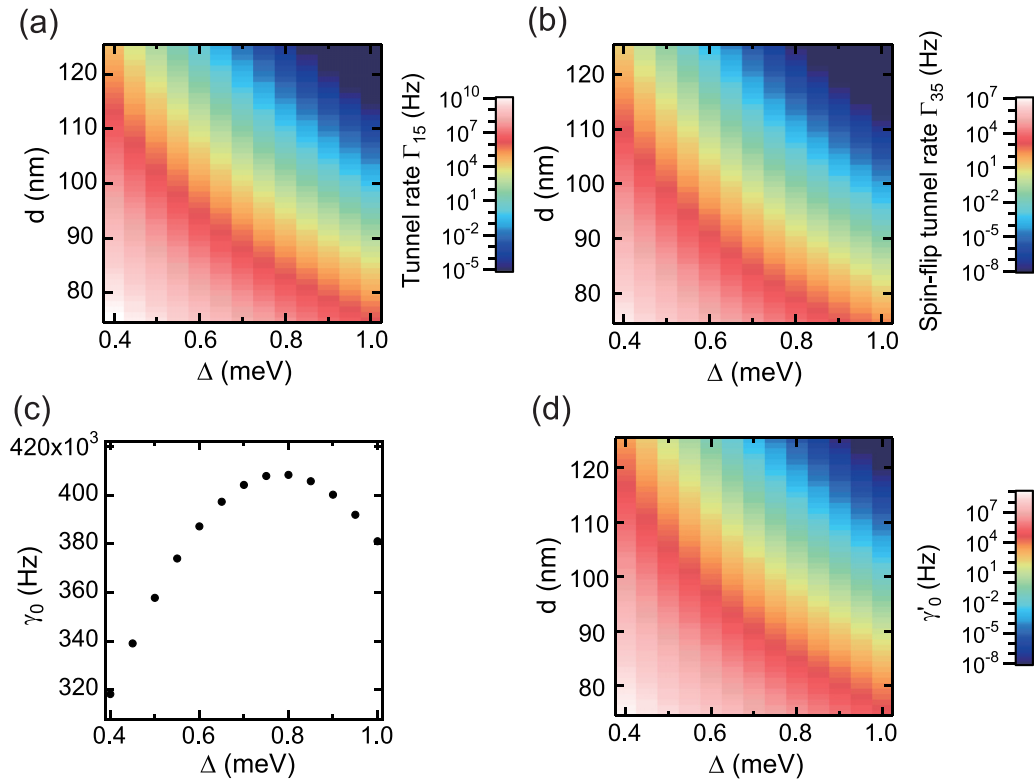


FIG. 4. (a) Color-coded map of the spin-conserving tunnel rate  $\Gamma_{15}$  calculated for  $\Delta$  and  $d$ . (b) Color-coded map of the spin-flip tunnel rate  $\Gamma_{35}$  calculated for  $\Delta$  and  $d$ . (c)  $\gamma_0$  plotted with respect to the singlet-triplet energy separation  $\Delta$ . (d) Color-coded map of  $\gamma'_0$  plotted in the plane of  $\Delta$  and  $d$ .

from state 3 to 6 and from state 4 to 7 start to take place frequently, and  $\Gamma_{R \leftarrow L}$  increases with increasing  $T_L$ . Similarly,  $\Gamma_{L \leftarrow R}$  is plotted as functions of  $T_L$  and  $T_R$  in the color-coded map of Fig. 5(b) and increases above about  $T_R = 2$  K due to the frequent phonon-mediated spin-flip excitations from state 5 to states 6 and 7.

A more intriguing feature appears in the temperature dependence of the ratio of  $\Gamma_{L \leftarrow R}/\Gamma_{R \leftarrow L}$ . We plot it with respect to  $T_L$  and  $T_R$  in the color-coded map shown in Fig. 5(c). The map can be divided into five characteristic regions: When  $T_L, T_R < 2$  K, the ratio is constant at 2, which is simply determined by the ratio of  $\Gamma_{35} + \Gamma_{45}$  to  $\Gamma_{53}$ . When  $T_L < 2$  K and  $T_R > 2$  K, the phonon excitation processes take place only in the right QD. Therefore, only  $\Gamma_{L \leftarrow R}$  increases, and the ratio  $\Gamma_{L \leftarrow R}/\Gamma_{R \leftarrow L}$  increases accordingly. In contrast, when  $T_L > 2$  K and  $T_R < 2$  K, the phonon excitation processes take place only in the left QD. Therefore, only  $\Gamma_{R \leftarrow L}$  increases, and the ratio decreases accordingly. For  $T_R > T_L > 2$  K, the ratio is larger than that in the equilibrium condition of  $T_L = T_R$ . This behavior can be understood by the fact that the phonon excitation in the right QD is more frequent than that in the left QD. For  $T_L > T_R > 2$  K, the behavior is reversed. To show the imbalance of the spin-flip tunnel rates more clearly, we plot the  $\Gamma_{L \leftarrow R}/\Gamma_{R \leftarrow L}$  vs.  $T_R$  for different temperature gradients, i.e.,  $T_L = rT_R$ , in Fig. 5(d). First, for the equilibrium case of  $r = 1$ , the ratio stays at 2 for low temperatures and decreases above around 1 K. Note that the factor 2 is originated from the ratio of  $(\Gamma_{35} + \Gamma_{45})/\Gamma_{53}$ . Furthermore, the ratio  $\Gamma_{L \leftarrow R}/\Gamma_{R \leftarrow L}$  approaches 2/3 at higher  $T_L$ . This is explained by the fact that states 5, 6, and 7 are equally populated at higher  $T_L$  and  $T_R$

and that  $\gamma'_0 \gg \Gamma_{35}, \Gamma_{53}$ . Thus, the value of 2/3 is determined by the proportion of the occupation probability of either state 6 or 7 out of states 5, 6, and 7. For  $T_L < T_R$ , the ratio is clearly different from the behavior of the equilibrium case and increases at  $T_L > 1$  K. The increase of the ratio is larger for the smaller  $r$ , i.e., larger temperature gradient between the QDs. For  $T_L > T_R$ , the ratio can be smaller than 2/3 when the temperature gradient is larger.

## V. OCCUPATION PROBABILITIES OF THE TWO-ELECTRON SPIN STATES

Next, we calculated the occupation probabilities of the respective spin states, [refer to the transition diagram in Fig. 2(b)] for different values of  $T_L$  and  $T_R$ . We considered the occupation probabilities of either  $|S(0, 2)\rangle$ ,  $|T_{\pm}(0, 2)\rangle$ , or  $|T_0(0, 2)\rangle$  in the  $(0, 2)$  charge state,  $P_{02} \equiv P_5 + P_6 + P_7 + P_8$ , and those of the anti-parallel spin states  $P_{AP} \equiv P_1 + P_2$ , and the parallel spin states,  $P_P \equiv P_3 + P_4$ , in the  $(1, 1)$  charge state, where  $P_i$  ( $i = 1, \dots, 8$ ) denotes the occupation probability of state  $i$  in the transition diagram in Fig. 2(b). Figures 6(a)–6(c) show the color-coded maps of  $P_{02}$ ,  $P_{AP}$ , and  $P_P$ , respectively. When  $T_L, T_R < 2$  K, since the occupations of the ground states dominate,  $P_{02} = 0.2$ , and  $P_{AP}, P_P = 0.4$ . In the case of  $T_R > T_L > 2$  K,  $P_{AP}$  decreases, and  $P_P$  increases. This behavior is explained by more phonon excitation from state 5 to either 6 or 7 and the imbalance between  $\Gamma_{36}$  and  $\Gamma_{63}$  and between  $\Gamma_{47}$  and  $\Gamma_{74}$  (i.e.,  $\Gamma_{36} > \Gamma_{63}$  and  $\Gamma_{47} > \Gamma_{74}$ ). Thus, states 3 and 4 are more populated by the phonon-mediated spin-flip transition from state 5 to 3 via state 6 or

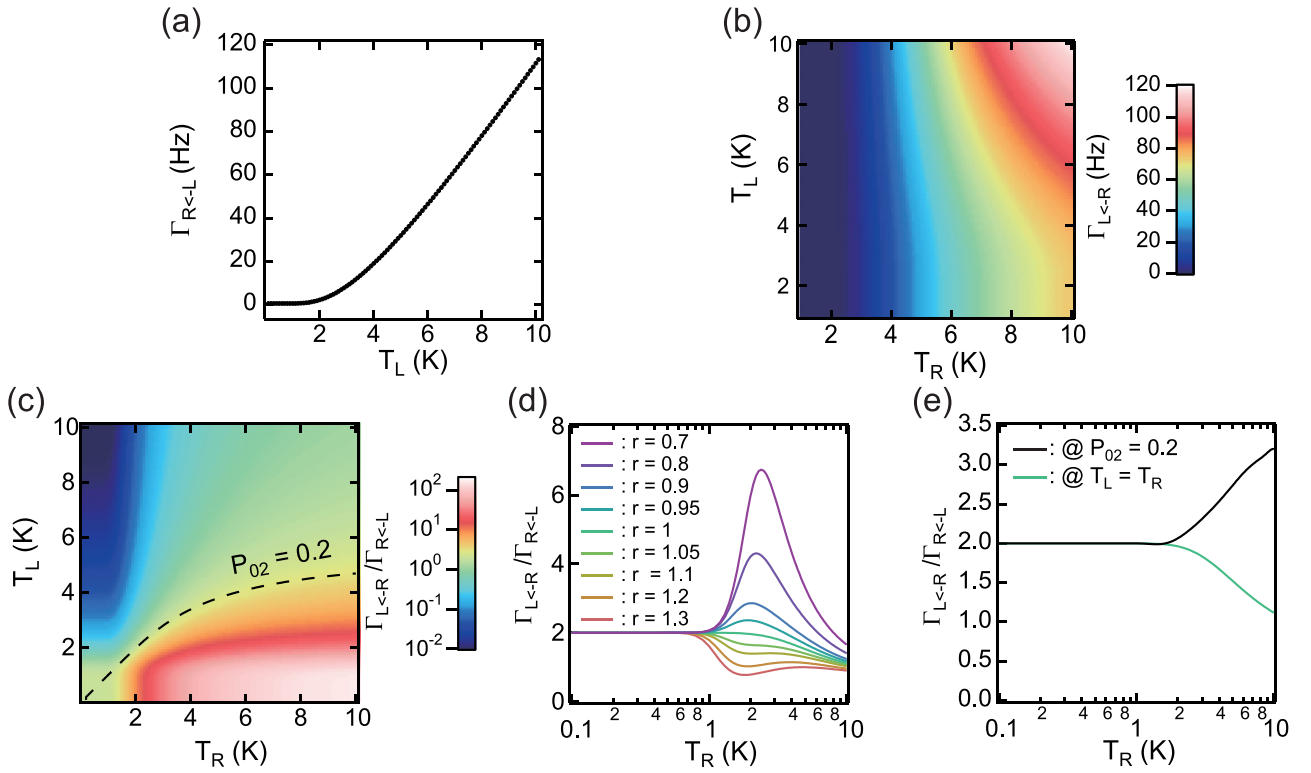


FIG. 5. (a) Spin-flip tunnel rate from the left to right QD,  $\Gamma_{R\leftarrow L}$ , plotted as a function of  $T_L$ . (b) Color-coded map of the spin-flip tunnel rate from the right to left QD,  $\Gamma_{L\leftarrow R}$ , plotted as functions of  $T_L$  and  $T_R$ . (c) Color-coded map of the spin-flip rate ratio,  $\Gamma_{L\leftarrow R}/\Gamma_{R\leftarrow L}$ , plotted with respect to  $T_L$  and  $T_R$ . A dashed line indicates  $T_L$  and  $T_R$  satisfying  $P_{02} \sim 0.2$  [see Fig. 6(a)]. (d)  $\Gamma_{L\leftarrow R}/\Gamma_{R\leftarrow L}$  ratio for various temperature gradients, i.e.,  $T_L = rT_R$ , plotted as a function of  $T_R$ . The colors correspond to the values of  $r$  as shown in the annotation in the figure. (e)  $\Gamma_{L\leftarrow R}/\Gamma_{R\leftarrow L}$  ratio extracted from 5(c) at  $P_{02} \sim 0.2$  [see a dashed line in (c) and Fig. 6(a)] is plotted by a black line. The same ratio at the equilibrium condition, i.e.,  $T_L = T_R$ , is plotted by a green line, as a reference.

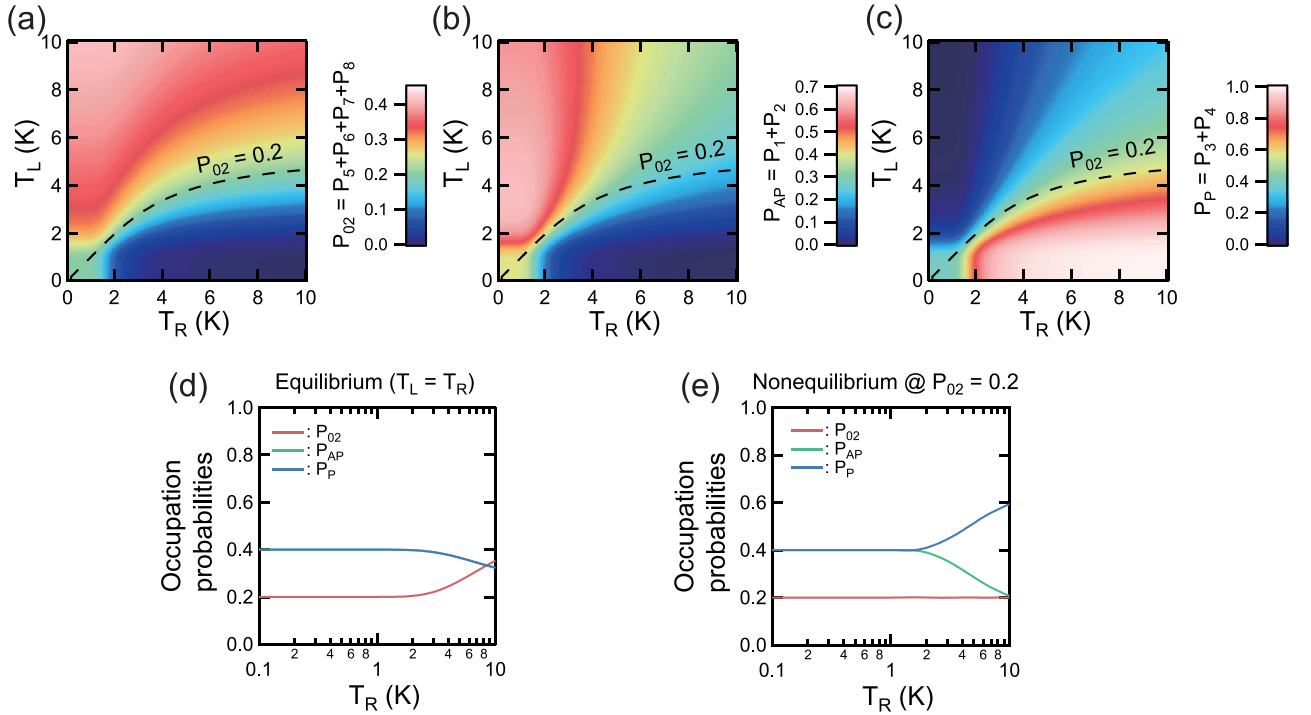


FIG. 6. [(a)–(c)] Color-coded maps of  $P_{02}$ ,  $P_{AP}$ , and  $P_P$ , respectively, calculated for  $T_L$  and  $T_R$ . (d)  $P_{02}$  (red),  $P_{AP}$  (green), and  $P_P$  (blue) plotted as a function of  $T_R$  under the equilibrium condition, i.e.,  $T_L = T_R$ .  $P_{AP}$  and  $P_P$  take the same value. (e)  $P_{AP}$  and  $P_P$  extracted from (b) and (c), respectively, at  $P_{02} \sim 0.2$  [see a dashed line in [(a)–(c)]].

from state 5 to 4 via state 7. On the other hand, in the case of  $T_L > T_R > 2$  K, since more phonon excitation from state 3 (4) to state 6 (7) takes place, and state 3 (4) is depopulated, resulting in the increase of the occupation probability of either state 1 or 2,  $P_{AP}$ , and of the probability of the (0, 2) charge state,  $P_{02}$ . Next, we considered the equilibrium case, i.e.,  $T_L = T_R$ , and the occupation probabilities  $P_{02}$ ,  $P_{AP}$ , and  $P_P$  are shown in Fig. 6(d). Note that  $P_{AP}$  and  $P_P$  overlap completely in the equilibrium condition. Above  $T_R = 2$  K,  $P_{AP}$  and  $P_P$  start to decrease from 0.4 while  $P_{02}$  increases from 0.2.

In our previous experiment, (see Fig. 4(b) in Ref. [12]),  $P_{02}$  was constant at around 0.2, while  $P_{AP}$  decreased and  $P_P$  increased from 0.4. These behaviors of the occupation probabilities are clearly different from those calculated in the equilibrium condition shown in Fig. 6(d). In order to compare the theoretically calculated occupation probabilities with the experimental result, we extract the  $P_{AP}$  and  $P_P$  for  $T_L$  and  $T_R$  that satisfy  $P_{02} \sim 0.2$  (see a dashed line in Fig. 6(a)). Figure 6(e) shows  $P_{02}$ ,  $P_{AP}$ , and  $P_P$  along the dashed line. Unlike the equilibrium case shown in Fig. 6(d), while  $P_{AP}$  decreases above  $T_R = 2$  K, and  $P_P$  increases around the same temperature. These behaviors of  $P_{AP}$  and  $P_P$  are in very good agreement with our experimental result. We can conclude that the characteristic imbalance of the occupation probability between parallel and anti-parallel spin configurations shown in Ref. [12] was not caused by the phonon temperature increase but by the phonon temperature gradient in the DQD system. In addition, the black dashed line of  $P_{02}(T_L, T_R) = 0.2$  in Fig. 6(a) predicts what kind of phonon temperature gradient was actually generated by a nearby phonon source QD [12].

Finally, we make a brief comment on the ratio of  $\Gamma_{L \leftarrow R}$  to  $\Gamma_{R \leftarrow L}$ . As mentioned in the previous paragraph, our previous experimental study showed  $P_{02}(T_L, T_R) \sim 0.2$  for all values of a bias voltage applied on a nearby phonon source QD. Therefore, we calculated the ratio as a function of  $T_R$  under the condition of  $P_{02}(T_L, T_R) \sim 0.2$ , as shown by a black line in Fig. 5(e). A green line in Fig. 5(e) is the ratio calculated at the equilibrium condition, i.e.,  $T_L = T_R$ , extracted from Fig. 5(d) and is shown as a reference data. The ratio  $\Gamma_{L \leftarrow R}/\Gamma_{R \leftarrow L}$  calculated under the nonequilibrium condition increases above  $T_R = 2$  K, while that of the equilibrium condition decreases. Although in our previous study [12], we plotted the ratio as a function of the applied bias voltage of a nearby phonon source QD instead of the phonon temperatures, this behavior of  $\Gamma_{L \leftarrow R}/\Gamma_{R \leftarrow L}$  is in good agreement with our experimental result as well (see Fig. S5 in Supplemental Material of Ref. [12]).

## VI. CONCLUSION

In conclusion, we theoretically investigated the phonon-mediated spin-flip tunnel processes in the two-electron DQD under a phonon temperature gradient over the DQD, to reproduce our previous experimental result [12]. The spin-flip tunnel processes via the  $|T_{\pm}(0, 2)\rangle$  states are strongly enhanced when the thermal energy of acoustic phonons exceeds the excitation energy of the triplet states. Furthermore, the spin-flip tunnel rates in opposite tunneling directions to each other is significantly affected by the phonon temperature gradient. The occupation probabilities of the respective spin

states are significantly modified as well by the phonon temperature gradient. These behaviors are in excellent agreement with our previous experimental result. In addition, the calculations regarding the occupation probabilities indicates that as long as  $P_{02}(T_L, T_R)$  is kept at a certain constant value like our previous experiment, the DQD in the nonequilibrium environment realizes a spin-pumping-like effect that makes either the parallel spin state or antiparallel spin state in the (1, 1) charge state more occupied. Since the spin-pumping-like effect can be regarded as thermodynamic work conducting on spins by a heat flow at the DQD, our DQD system can work as mesoscopic heat engines using single spins as working substances. If the phonon temperatures in QDs can be controlled individually in the coupled QD systems, more interesting spin-related thermodynamic functions of QDs would be realized.

## ACKNOWLEDGMENTS

This work was supported by Grant-in-Aid for Scientific Research (S) (No. JP19H05610), JST CREST (No. JPMJCR15N2 and JPMJCR1675), JST Moonshot R&D grant (No. JPMJMS226B), MEXT Quantum Leap Flagship Program grant (No. JPMXS0118069228), Grant-in-Aid for Young Scientists (No. JP20K14384), and Grant-in-Aid for JSPS Fellows (No. JP16J03037, No. JP19J01737). K.K. acknowledges JST, PRESTO (Grant No. JPMJPR2255) and the Murata Science Foundation. S.M. acknowledges JST FOREST (Grant No. JPMJFR223A) and the Murata Science Foundation. Y.T. is supported by Grant-in-Aid for Scientific Research (C) (No. JP18K03479) and JST Moonshot R&D-MILLENNIA Program (Grant No. JPMJMS2061).

## APPENDIX A: HAMILTONIAN OF THE TWO-ELECTRON DQD SYSTEM WITH THE SPIN-ORBIT INTERACTION

We considered the two-electron spin configurations of the (1, 1) and (0, 2) charge states in the DQD. The geometry of the DQD is illustrated in Fig. 1. For the parameters defining the DQD, we refer to our previous experiment [12]. The two QDs are aligned along the GaAs crystallographic orientation of [01-1]. An in-plane magnetic field  $B$  is applied along the [0-1-1] direction. The total Hamiltonian of the two-electron system is

$$\hat{H} = \hat{H}_{\text{QD}_{2e}} + \hat{H}_{\text{ph}} + \hat{H}_{e\text{-p}}, \quad (\text{A1})$$

where  $\hat{H}_{\text{QD}_{2e}}$  is the Hamiltonian of two electrons in the DQD.  $\hat{H}_{\text{ph}}$  and  $\hat{H}_{e\text{-p}}$  are the phonon Hamiltonian and the electron-phonon interaction, respectively. In this section, we derive the Hamiltonian matrix of  $\hat{H}_{\text{QD}_{2e}}$  in the end. First, we define the Hamiltonian of an electron in the DQD system,  $\hat{H}_{\text{QD}_{1e}}$ , as

$$\hat{H}_{\text{QD}_{1e}} = \hat{H}_0 + \hat{H}_Z + \hat{H}_{\text{so}} + \hat{H}_{\text{det}}, \quad (\text{A2})$$

where  $\hat{H}_0$  represents the kinetic energy and the potential energy of an electron in the DQD. The Zeeman term and the spin-orbit interaction are denoted as  $\hat{H}_Z$  and  $\hat{H}_{\text{so}}$ , respectively.  $\hat{H}_{\text{det}} = eEx$  is an energy detuning between the QDs induced by a linear electric field  $E$  applied across the DQD. Here, we



define  $\hat{\mathcal{H}}_0$  in the  $xy$  plane as

$$\hat{\mathcal{H}}_0 = -\frac{\hbar^2}{2m^*} \left( \frac{\partial^2}{\partial x^2} + \frac{\partial^2}{\partial y^2} \right) + V(x, y).$$

We consider a parabolic electrostatic potential  $V(\mathbf{r})$ , with the local minima at  $\mathbf{r} = (\pm d, 0)$ :

$$V(x, y) = \frac{\hbar^2}{2m^*l_0^4} \min\{(\mathbf{r} - \mathbf{d})^2, (\mathbf{r} + \mathbf{d})^2\}, \quad (\text{A3})$$

where  $l_0$  is the confinement length of an electron in the QD, typically 30 to 100 nm, and  $m^* = 0.067m_0$  is the effective mass of electrons in GaAs. Note that the spatial shift of the potential minima induced by  $\hat{\mathcal{H}}_{\text{det}}$  is dismissed in our calculation [29]. It also should be noted that we set the external magnetic field  $B$  to be sufficiently small ( $\sim 0.1$  T) such that a magnetic confinement energy is negligible compared to the original QD confinement energy  $\hbar\omega_0 = \hbar^2/(m^*l_0^2)$ . Therefore,  $B$  only defines the spin eigenstates by the Zeeman effect.

The Hamiltonian of the Zeeman term is described as  $\hat{\mathcal{H}}_Z = (g\mu_B/2)\mathbf{B} \cdot \hat{\boldsymbol{\sigma}}$ , where  $g$  and  $\mu_B$  are the Lande  $g$  factor of an electron spin in the QD and the Bohr magneton, respectively.  $\hat{\boldsymbol{\sigma}}$  is the vector of the Pauli-spin operators. Furthermore, we make a comment on a local Zeeman energy induced by the Overhauser field of nuclear spins, inducing the energy difference between  $|\uparrow\downarrow(1, 1)\rangle$  and  $|\downarrow\uparrow(1, 1)\rangle$ . In previous studies [30], a nuclear field is typically 1–5 mT. In such a case, for a weakly coupled DQD, the Zeeman energy difference between the two dots becomes comparable with the exchange energy difference between  $|S(1, 1)\rangle$  and  $|T_0(1, 1)\rangle$ . Therefore, the eigenstates of the antiparallel spin configurations of the  $(1, 1)$  charge state are not  $|S(1, 1)\rangle$  and  $|T_0(1, 1)\rangle$  but  $|\uparrow\downarrow(1, 1)\rangle$  and  $|\downarrow\uparrow(1, 1)\rangle$ . In addition, it is assumed that the Zeeman energy originated from the external  $B$  field is much stronger than that of the local nuclear field and the exchange energy for  $|S(1, 1)\rangle$  and  $|T_0(1, 1)\rangle$ . Therefore, it is safely assumed that  $|T_{\pm}(1, 1)\rangle$  are good quantum basis in this configuration of the weakly coupled DQD system.

The two-electron wave functions involved in the phonon-mediated spin-flip processes are defined, by using a single electron wavefunction of the  $1s$  orbital in the left QD,  $\tilde{\psi}_L(\mathbf{r})$ , and that of the  $1s$  and  $2p$  orbitals in the right QD,  $\tilde{\psi}_R(\mathbf{r})$ , and  $\tilde{\psi}_{R^*}(\mathbf{r})$  (see Appendix B for the detailed expressions of the wave functions). The wave functions of  $|\uparrow\downarrow(1, 1)\rangle$ ,  $|\downarrow\uparrow(1, 1)\rangle$ ,  $|T_+(1, 1)\rangle$ ,  $|T_-(1, 1)\rangle$ ,  $|S(0, 2)\rangle$ ,  $|T_+(0, 2)\rangle$ ,  $|T_-(0, 2)\rangle$ , and  $|T_0(0, 2)\rangle$  are described as follows [see the transition diagram in Fig. 2(b)]:

$$\begin{aligned} \Psi_1 \equiv & \frac{1}{\sqrt{2}} (\tilde{\psi}_L(\mathbf{r}_1)\tilde{\psi}_R(\mathbf{r}_2)\chi_{\uparrow 1}\chi_{\downarrow 2} \\ & - \tilde{\psi}_R(\mathbf{r}_1)\tilde{\psi}_L(\mathbf{r}_2)\chi_{\downarrow 1}\chi_{\uparrow 2}), \end{aligned} \quad (\text{A4})$$

$$\begin{aligned} \Psi_2 \equiv & \frac{1}{\sqrt{2}} (\tilde{\psi}_R(\mathbf{r}_1)\tilde{\psi}_L(\mathbf{r}_2)\chi_{\uparrow 1}\chi_{\downarrow 2} \\ & - \tilde{\psi}_L(\mathbf{r}_1)\tilde{\psi}_R(\mathbf{r}_2)\chi_{\downarrow 1}\chi_{\uparrow 2}), \end{aligned} \quad (\text{A5})$$

$$\Psi_3 \equiv \frac{1}{\sqrt{2}} (\tilde{\psi}_L(\mathbf{r}_1)\tilde{\psi}_R(\mathbf{r}_2) - \tilde{\psi}_R(\mathbf{r}_1)\tilde{\psi}_L(\mathbf{r}_2))\chi_{T+}, \quad (\text{A6})$$

$$\Psi_4 \equiv \frac{1}{\sqrt{2}} (\tilde{\psi}_L(\mathbf{r}_1)\tilde{\psi}_R(\mathbf{r}_2) - \tilde{\psi}_R(\mathbf{r}_1)\tilde{\psi}_L(\mathbf{r}_2))\chi_{T-}, \quad (\text{A7})$$

$$\Psi_5 \equiv \tilde{\psi}_R(\mathbf{r}_1)\tilde{\psi}_R(\mathbf{r}_2)\chi_S, \quad (\text{A8})$$

$$\Psi_6 \equiv \frac{1}{\sqrt{2}} (\tilde{\psi}_R(\mathbf{r}_1)\tilde{\psi}_{R^*}(\mathbf{r}_2) - \tilde{\psi}_{R^*}(\mathbf{r}_1)\tilde{\psi}_R(\mathbf{r}_2))\chi_{T+}, \quad (\text{A9})$$

$$\Psi_7 \equiv \frac{1}{\sqrt{2}} (\tilde{\psi}_R(\mathbf{r}_1)\tilde{\psi}_{R^*}(\mathbf{r}_2) - \tilde{\psi}_{R^*}(\mathbf{r}_1)\tilde{\psi}_R(\mathbf{r}_2))\chi_{T-}, \quad (\text{A10})$$

$$\Psi_8 \equiv \frac{1}{\sqrt{2}} (\tilde{\psi}_R(\mathbf{r}_1)\tilde{\psi}_{R^*}(\mathbf{r}_2) - \tilde{\psi}_{R^*}(\mathbf{r}_1)\tilde{\psi}_R(\mathbf{r}_2))\chi_{T0}, \quad (\text{A11})$$

where  $\chi_S$  and  $\chi_{T_v}$  represent the spin wave functions of the spin triplet and singlet states, respectively. To describe the spin wave functions, we define  $\chi_{\uparrow i}$  and  $\chi_{\downarrow i}$  for  $i = 1, 2$ , which denote the spin wave functions of the  $i$ -th electron spin and satisfy  $\chi_{\uparrow i}^\dagger\chi_{\uparrow j} = \chi_{\downarrow i}^\dagger\chi_{\downarrow j} = \delta_{ij}$  and  $\chi_{\uparrow i}^\dagger\chi_{\downarrow j} = 0$ . Then, the spin wave functions of the spin singlet  $\chi_S$  and triplet states  $\chi_{T_v}$  are described as follows:

$$\chi_S \equiv \frac{1}{\sqrt{2}} (\chi_{\uparrow 1}\chi_{\downarrow 2} - \chi_{\downarrow 1}\chi_{\uparrow 2}), \quad (\text{A12})$$

$$\chi_{T+} = \chi_{\uparrow 1}\chi_{\uparrow 2}, \quad (\text{A13})$$

$$\chi_{T0} = \frac{1}{\sqrt{2}} (\chi_{\uparrow 1}\chi_{\downarrow 2} + \chi_{\downarrow 1}\chi_{\uparrow 2}), \quad (\text{A14})$$

$$\chi_{T-} = \chi_{\downarrow 1}\chi_{\downarrow 2}. \quad (\text{A15})$$

Note that the spin-quantization axis is selected to be parallel to the in-plane magnetic field,  $\mathbf{B}$  [(see Fig. 1(a)]. The two-electron Hamiltonian without the spin-orbit interaction is  $\hat{\mathcal{H}}_{0Z,2e} \equiv \sum_{i=1,2} \{\hat{\mathcal{H}}_0^{(i)} + \hat{\mathcal{H}}_Z^{(i)} + \hat{\mathcal{H}}_{\text{det}}^{(i)}\} + \hat{\mathcal{H}}_{\text{int}}$ , where  $\hat{\mathcal{H}}_{\text{int}}$  represents the Coulomb interaction. Then, the diagonal matrix elements of  $\hat{\mathcal{H}}_{0Z,2e}$  are

$$\langle \Psi_1 | \hat{\mathcal{H}}_{0Z,2e} | \Psi_1 \rangle = \epsilon_L + \epsilon_R + V, \quad (\text{A16})$$

$$\langle \Psi_2 | \hat{\mathcal{H}}_{0Z,2e} | \Psi_2 \rangle = \epsilon_L + \epsilon_R + V, \quad (\text{A17})$$

$$\langle \Psi_3 | \hat{\mathcal{H}}_{0Z,2e} | \Psi_3 \rangle = \epsilon_L + \epsilon_R + V + g\mu_B B, \quad (\text{A18})$$

$$\langle \Psi_4 | \hat{\mathcal{H}}_{0Z,2e} | \Psi_4 \rangle = \epsilon_L + \epsilon_R + V - g\mu_B B, \quad (\text{A19})$$

$$\langle \Psi_5 | \hat{\mathcal{H}}_{0Z,2e} | \Psi_5 \rangle = 2\epsilon_R + \epsilon_{\text{det}} + U, \quad (\text{A20})$$

$$\langle \Psi_6 | \hat{\mathcal{H}}_{0Z,2e} | \Psi_6 \rangle = \epsilon_R + \epsilon_{R^*} + \epsilon_{\text{det}} + U' + g\mu_B B, \quad (\text{A21})$$

$$\langle \Psi_7 | \hat{\mathcal{H}}_{0Z,2e} | \Psi_7 \rangle = \epsilon_R + \epsilon_{R^*} + \epsilon_{\text{det}} + U' - g\mu_B B, \quad (\text{A22})$$

$$\langle \Psi_8 | \hat{\mathcal{H}}_{0Z,2e} | \Psi_8 \rangle = \epsilon_R + \epsilon_{R^*} + \epsilon_{\text{det}} + U'. \quad (\text{A23})$$

where  $V$  and  $U$  are the inter- and intra-QD charging energy, respectively.  $U' = U - K$ , where  $K (> 0)$  is the change in the Coulomb interaction energy between  $|S(0, 2)\rangle$  and  $|T_v(0, 2)\rangle$  [20].  $\epsilon_L$  and  $\epsilon_R$  are the eigenenergies of the left and right QDs, and  $\epsilon_{R^*}$  is that of the first excited state in the right QD (see Appendix B).  $\epsilon_{\text{det}} \simeq 2eEd$  is the energy detuning between the  $(1, 1)$  and  $(0, 2)$  charge states. Note that the dependence of the intra-QD charging energy on the wave functions  $\tilde{\psi}_L$ , and  $\tilde{\psi}_R$  is neglected. The off-diagonal matrix elements of  $\hat{\mathcal{H}}_{0Z,2e}$ , which

represent the interdot tunnel coupling, are

$$\langle \Psi_1 | \hat{\mathcal{H}}_{0Z_{2e}} | \Psi_5 \rangle = \langle \Psi_2 | \hat{\mathcal{H}}_{0Z_{2e}} | \Psi_5 \rangle = \tau_{LR}, \quad (\text{A24})$$

$$\langle \Psi_3 | \hat{\mathcal{H}}_{0Z_{2e}} | \Psi_6 \rangle = \langle \Psi_4 | \hat{\mathcal{H}}_{0Z_{2e}} | \Psi_7 \rangle = -\tau_{LR^*}, \quad (\text{A25})$$

and

$$\langle \Psi_1 | \hat{\mathcal{H}}_{0Z_{2e}} | \Psi_8 \rangle = -\langle \Psi_2 | \hat{\mathcal{H}}_{0Z_{2e}} | \Psi_8 \rangle = -\tau_{LR^*}/\sqrt{2}. \quad (\text{A26})$$

The definitions of  $\tau_{LR}$  and  $\tau_{LR^*}$  are described in Appendix B. Finally, the Hamiltonian of the spin-orbit interaction is

$$\begin{aligned} \hat{\mathcal{H}}_{so} = & \frac{\hbar}{m^* \lambda_D} (-\hat{p}_{x'} \hat{\sigma}_{x'} + \hat{p}_{y'} \hat{\sigma}_{y'}) \\ & + \frac{\hbar}{m^* \lambda_R} (\hat{p}_{x'} \hat{\sigma}_{y'} - \hat{p}_{y'} \hat{\sigma}_{x'}), \end{aligned} \quad (\text{A27})$$

where  $\lambda_D$  and  $\lambda_R$  are the spin-orbit lengths for the Dresselhaus and Rashba interactions, respectively. The  $x'$  and  $y'$  axis are set along [010] and [001] in GaAs, respectively, as depicted in Fig. 1. The angle between the  $x$  and  $x'$  axis is denoted by  $\delta$ . The coordinates of the  $xy$  and  $x'y'$  planes can be transformed as  $(x', y') = (x \cos \delta + y \sin \delta, -x \sin \delta + y \cos \delta)$ , using the angle  $\delta$ . In the  $xy$  plane, the spin-orbit interaction Hamiltonian is simply given by (see Appendix C for the derivation)

$$\hat{\mathcal{H}}_{so} = -\frac{\hbar}{m^*} \left[ \frac{\cos 2\delta}{\lambda_D} \hat{p}_x \hat{\sigma}_y + \left( \frac{\sin 2\delta}{\lambda_D} - \frac{1}{\lambda_R} \right) \hat{p}_y \hat{\sigma}_y \right]. \quad (\text{A28})$$

In our previous experimental study in Ref. [12],  $\delta = \pi/4$  was chosen. In this condition, the off-diagonal elements involved in the spin-orbit interaction can be described by

$$\langle \Psi_3 | \sum_{i=1,2} \hat{\mathcal{H}}_{so}^{(i)} | \Psi_5 \rangle = \langle \Psi_4 | \sum_{i=1,2} \hat{\mathcal{H}}_{so}^{(i)} | \Psi_5 \rangle = \frac{\hbar^2 d_{ID}}{m^* \lambda_{so}}, \quad (\text{A29})$$

where  $i = 1, 2$ , which represents the individual electrons in the DQD. The effective spin-orbit inverse-length is defined as  $\lambda_{so}^{-1} \equiv \lambda_R^{-1} - \lambda_D^{-1}$ . The interdot inverse dipole element,  $d_{ID}$ , is given as

$$d_{ID} \equiv \int d^2 \mathbf{r} \tilde{\psi}_L^*(\mathbf{r}) \frac{\partial}{\partial y} \tilde{\psi}_R(\mathbf{r}). \quad (\text{A30})$$

Similarly, the off-diagonal elements of  $\hat{\mathcal{H}}_{so}$  between  $|\Psi_5\rangle$  and  $|\Psi_6\rangle$  and between  $|\Psi_5\rangle$  and  $|\Psi_7\rangle$  are

$$\langle \Psi_6 | \sum_{i=1,2} \hat{\mathcal{H}}_{so}^{(i)} | \Psi_5 \rangle = \langle \Psi_7 | \sum_{i=1,2} \hat{\mathcal{H}}_{so}^{(i)} | \Psi_5 \rangle = -\frac{\hbar^2 d_R}{m^* \lambda_{so}}, \quad (\text{A31})$$

where the inverse dipole matrix element in the right QD,  $d_R$ , is

$$d_R \equiv \int d^2 \mathbf{r} \tilde{\psi}_R^*(\mathbf{r}) \frac{\partial}{\partial y} \tilde{\psi}_R(\mathbf{r}). \quad (\text{A32})$$

To summarize the above discussion, the Hamiltonian matrix of the two electrons in the laterally coupled DQD are expressed in terms of the basis states,  $(|\Psi_1\rangle; \dots; |\Psi_8\rangle)$ :

$$\begin{aligned} \hat{\mathcal{H}}_{QD_{2e}} = & \sum_{i=1,2} \{ \hat{\mathcal{H}}_0^{(i)} + \hat{\mathcal{H}}_Z^{(i)} + \hat{\mathcal{H}}_{so}^{(i)} + \hat{\mathcal{H}}_{det}^{(i)} \} + \hat{\mathcal{H}}_{int} \\ = & \begin{pmatrix} 0 & 0 & 0 & 0 & \tau_{LR} & 0 & 0 & -\tau_{LR^*}/\sqrt{2} \\ 0 & 0 & 0 & 0 & \tau_{LR} & 0 & 0 & \tau_{LR^*}/\sqrt{2} \\ 0 & 0 & E_Z & 0 & \alpha & -\tau_{LR^*} & 0 & 0 \\ 0 & 0 & 0 & -E_Z & \alpha & 0 & -\tau_{LR^*} & 0 \\ \tau_{LR}^* & \tau_{LR}^* & \alpha^* & \alpha^* & \epsilon & \beta & \beta & 0 \\ 0 & 0 & -\tau_{LR^*}^* & 0 & \beta^* & \epsilon' + E_Z & 0 & 0 \\ 0 & 0 & 0 & -\tau_{LR^*}^* & \beta^* & 0 & \epsilon' - E_Z & 0 \\ -\tau_{LR}^*/\sqrt{2} & \tau_{LR}^*/\sqrt{2} & 0 & 0 & 0 & 0 & 0 & \epsilon' \end{pmatrix}, \end{aligned} \quad (\text{A33})$$

where the diagonal elements are expressed as the difference from the reference energy,  $\epsilon_L + \epsilon_R + V$ . The Zeeman energy is described as  $E_Z \equiv g\mu_B B$ .  $\epsilon \equiv \epsilon_R - \epsilon_L + \epsilon_{det} + U - V$  is the energy detuning between  $|\Psi_1\rangle$  or  $|\Psi_2\rangle$  and  $|\Psi_5\rangle$ , and  $\epsilon' \equiv \epsilon_{R^*} - \epsilon_L + \epsilon_{det} + U' - V$  is that between  $|\Psi_1\rangle$  or  $|\Psi_2\rangle$  and  $|\Psi_8\rangle$ . Note that there is a local Zeeman energy difference between  $|\Psi_1\rangle$  and  $|\Psi_2\rangle$ , but since it is assumed that the local Zeeman energy difference is much smaller than  $E_Z$  and  $\Delta$ , it can be negligible in the Hamiltonian  $\hat{\mathcal{H}}_{QD_{2e}}$  and in the following calculation. The off-diagonal elements are  $\alpha \equiv \hbar^2 d_{ID}/(m^* \lambda_{so})$  and  $\beta \equiv -\hbar^2 d_R/(m^* \lambda_{so})$ . In the following derivations, we consider only the resonant condition where the energies of  $|\Psi_5\rangle$  and  $|\Psi_1\rangle$  are equivalent, i.e.,  $\epsilon = 0$ , by choosing  $\epsilon_{det}$  appropriately [see Fig. 2(a)]. Furthermore, in such a case, the energy separation between  $|\Psi_5\rangle$  and  $|\Psi_8\rangle$  is described as  $\Delta = \epsilon' = \epsilon_{R^*} - \epsilon_R - K$ .

By diagonalizing the matrix in Eq. (A33), we obtain the eigenenergies and corresponding two-electron wave func-

tions:  $\hat{\mathcal{H}}_{QD_{2e}} |\xi_n\rangle = E_n |\xi_n\rangle$ , where the eigenfunctions can be expanded as  $|\xi_n\rangle = \sum_{j=1}^8 C_{nj} |\Psi_j\rangle$ . Since the inter-QD tunnel coupling and the spin-orbit interactions are relatively weak, the off-diagonal elements of  $\hat{\mathcal{H}}_{QD_{2e}}$  are assumed to be very small. Therefore, the first-order perturbation theory can be applied to obtain the two-electron wave functions:  $C_{n,j} \simeq \langle \Psi_j | \hat{\mathcal{H}}_1 | \Psi_n \rangle / (E_n^0 - E_j^0)$  for  $n \neq j$ , and  $C_{n,n} = 1$ , where  $\hat{\mathcal{H}}_1$  is a matrix comprising the off-diagonal elements of  $\hat{\mathcal{H}}_{QD_{2e}}$ , and  $E_n^0$  is the  $n$ -th diagonal element of  $\hat{\mathcal{H}}_{QD_{2e}}$ .

## APPENDIX B: ELECTRON WAVE FUNCTIONS IN THE DQD

We assume that the Fock-Darwin states are suitable for representing the electron wave functions of the DQD [31–34]. The ground states in the left QD,  $\psi_L$ , those in the right

QD,  $\psi_R$ , and the first excited state in the right QD,  $\psi_{R^*}$  are

$$\psi_L(\mathbf{r}) = \frac{1}{\sqrt{\pi}l_0} \exp\left[-\frac{(x+d)^2 + y^2}{2l_0^2}\right], \quad (\text{B1})$$

$$\psi_R(\mathbf{r}) = \frac{1}{\sqrt{\pi}l_0} \exp\left[-\frac{(x-d)^2 + y^2}{2l_0^2}\right], \quad (\text{B2})$$

$$\psi_{R^*}(\mathbf{r}) = \psi_{R^*}^+(\mathbf{r}) \cos \phi_a + \psi_{R^*}^-(\mathbf{r}) e^{i\phi_b} \sin \phi_a, \quad (\text{B3})$$

respectively. For,  $\psi_{R^*}^\pm(\mathbf{r})$ , we use the linear combination of the wave functions of the  $2p$  orbitals:

$$\psi_{R^*}^\pm(\mathbf{r}) = \frac{x-d \pm iy}{\sqrt{\pi}l_0^2} \exp\left[-\frac{(x-d)^2 + y^2}{2l_0^2}\right]. \quad (\text{B4})$$

Considering the shape of the DQD potential in the sample used in Ref. [12], the wave function along the  $x$  axis has lower energy. Therefore, the wave functions of the excited states are assumed to expand along the  $x$  axis, i.e.,  $\phi_a \sim \pi/4$ , and  $\phi_b \sim 0$ . We chose  $\phi_a = \pi/4$  and  $\phi_b = 0.1\pi$  in such a way that  $\gamma'_0$ ,  $\Gamma_{15}$ , and  $\Gamma_{35}$  are in the same order as the values obtained in our previous study [12]. The Fock-Darwin wave functions of the different dots overlap each other, whereas the wave functions in the QDs should be orthogonal to each other. To avoid the overlaps, we introduced the extended Hund-Mulliken approach [29]. The wave functions having a small interdot overlap are mostly orthogonalized by the following treatments:

$$\tilde{\psi}_L(\mathbf{r}) \equiv \frac{1}{N_g} \left[ \psi_L(\mathbf{r}) - \frac{S}{2} \psi_R(\mathbf{r}) - 2S_p \psi_{R^*}(\mathbf{r}) \right], \quad (\text{B5})$$

$$\tilde{\psi}_R(\mathbf{r}) \equiv \frac{1}{N_g} \left[ \psi_R(\mathbf{r}) - \frac{S}{2} \psi_L(\mathbf{r}) \right], \quad (\text{B6})$$

$$\tilde{\psi}_{R^*}(\mathbf{r}) \equiv \frac{1}{N_e} [\psi_{R^*}(\mathbf{r}) + S_p \psi_L(\mathbf{r})], \quad (\text{B7})$$

where  $S$  and  $S_p$  are defined as

$$S \equiv \int d^2\mathbf{r} \psi_L^*(\mathbf{r}) \psi_R(\mathbf{r}), \quad (\text{B8})$$

$$S_p \equiv \int d^2\mathbf{r} \psi_L^*(\mathbf{r}) \psi_{R^*}(\mathbf{r}), \quad (\text{B9})$$

and  $N_g \simeq 1 - 3S^2/4$  and  $N_e \simeq 1 + S_p^2$  are the normalization coefficients. We note that these newly defined wave functions,  $\tilde{\psi}_L$ ,  $\tilde{\psi}_R$ , and  $\tilde{\psi}_{R^*}$ , are almost orthonormalized in the limit of the weak interdot coupling. For the  $z$  component of the wave functions,  $\psi_z(z)$ , the lowest eigenstate of the rectangular well model with infinite barriers is considered with the quantum well length  $l_z$ . The wave function is described as  $\psi_z(z) = \sqrt{2/l_z} \cos(\pi z/l_z)$ , where  $-l_z/2 \leq z \leq l_z/2$ . The  $z$  component of the wave functions,  $\psi_z$ , is multiplied to the wave functions of the  $xy$  plane, Eqs. (B5)–(B7), for the calculation of the electron-phonon interaction, because  $\psi_z$  involves the momentum matching between an electron and a phonon in the electron-phonon interaction. For simplicity, the wave function  $\psi_z$  is omitted in the following expressions.

The eigenenergies of the ground states in the left and right QDs,  $\epsilon_L$  and  $\epsilon_R$ , and that of the first excited state in the right QD,  $\epsilon_{R^*}$ , are calculated by using  $\hat{\mathcal{H}}_0$  as

$$\int d^2\mathbf{r} \tilde{\psi}_L^*(\mathbf{r}) \hat{\mathcal{H}}_0(\mathbf{r}) \tilde{\psi}_L(\mathbf{r}) \equiv \epsilon_L, \quad (\text{B10})$$

$$\int d^2\mathbf{r} \tilde{\psi}_R^*(\mathbf{r}) \hat{\mathcal{H}}_0(\mathbf{r}) \tilde{\psi}_R(\mathbf{r}) \equiv \epsilon_R, \quad (\text{B11})$$

$$\int d^2\mathbf{r} \tilde{\psi}_{R^*}^*(\mathbf{r}) \hat{\mathcal{H}}_0(\mathbf{r}) \tilde{\psi}_{R^*}(\mathbf{r}) \equiv \epsilon_{R^*}. \quad (\text{B12})$$

The off-diagonal matrix elements of  $\hat{\mathcal{H}}_0$  represent the tunnel coupling between the ground states in the two dots,  $\tau_{LR}$ , and that between the ground state in the left QD and the first-excited state in the right QD,  $\tau_{LR^*}$ :

$$\int d^2\mathbf{r} \tilde{\psi}_L^*(\mathbf{r}) \hat{\mathcal{H}}_0(\mathbf{r}) \tilde{\psi}_R(\mathbf{r}) \equiv \tau_{LR}, \quad (\text{B13})$$

$$\int d^2\mathbf{r} \tilde{\psi}_L^*(\mathbf{r}) \hat{\mathcal{H}}_0(\mathbf{r}) \tilde{\psi}_{R^*}(\mathbf{r}) \equiv \tau_{LR^*}, \quad (\text{B14})$$

where the parameters  $\tau_{LR}$ , and  $\tau_{LR^*}$  are complex numbers in general.

Furthermore, the energy separation between  $|S(0, 2)\rangle$  and  $|T_0(0, 2)\rangle$ ,  $\Delta$ , is determined by the summation of the orbital spacing  $\hbar\omega_0$  in the QD and the Coulomb interaction between two electrons [35]. By using the ratio of  $\Delta$  to the QD orbital spacing  $\hbar\omega_0$ ,  $\delta_{ST}$ , the electron confinement length in the QD,  $l_0$ , is determined by  $\Delta$  and  $\delta_{ST}$ :

$$l_0 = \sqrt{\frac{\hbar}{m^*\omega_0}} = \hbar \sqrt{\frac{\delta_{ST}}{m^*\Delta}}. \quad (\text{B15})$$

According to Ref. [35], the value of  $\delta_{ST}$  is determined by the confinement length of an electron in the QD  $l_0$  and the Bohr radius defined by the Coulomb interaction. For the calculations in this paper, we adopted the typical reported value of the ratio  $\delta_{ST} \sim 0.5$  [36].

### APPENDIX C: SPIN-ORBIT INTERACTIONS

For the Dresselhaus-type spin-orbit interaction, the momentum terms in the  $xy$  plane are

$$\begin{aligned} \hat{p}_x \hat{\sigma}_x + \hat{p}_y \hat{\sigma}_y &= -\hat{p}_x \hat{\sigma}_x \cos 2\delta + \hat{p}_x \hat{\sigma}_y \sin 2\delta \\ &\quad + \hat{p}_y \hat{\sigma}_x \sin 2\delta + \hat{p}_y \hat{\sigma}_y \cos 2\delta. \end{aligned} \quad (\text{C1})$$

The Rashba-type spin-orbit interaction is transformed to the expression in the  $xy$  plane:

$$\hat{p}'_x \hat{\sigma}'_y - \hat{p}'_y \hat{\sigma}'_x = \hat{p}_x \hat{\sigma}_y - \hat{p}_y \hat{\sigma}_x. \quad (\text{C2})$$

Thus,

$$\begin{aligned} \hat{\mathcal{H}}_{\text{so}} &= \frac{\hbar}{m^*} \left[ -\frac{\cos 2\delta}{\lambda_D} \hat{p}_x \hat{\sigma}_x + \left( \frac{\sin 2\delta}{\lambda_D} + \frac{1}{\lambda_R} \right) \hat{p}_x \hat{\sigma}_y \right. \\ &\quad \left. \times \left( \frac{\sin 2\delta}{\lambda_D} - \frac{1}{\lambda_R} \right) \hat{p}_y \hat{\sigma}_x + \frac{\cos 2\delta}{\lambda_D} \hat{p}_y \hat{\sigma}_y \right]. \end{aligned} \quad (\text{C3})$$

Because the  $B$  field is applied along the  $-y$  axis, the spin is oriented to the same direction. Therefore, the terms including  $\hat{\sigma}_y$  do not contribute to the spin-flip process and can be dismissed. Summing up the transformations, the spin-orbit

interaction Hamiltonian in the  $xy$  plane is described as

$$\hat{H}_{\text{so}} = \frac{\hbar}{m^*} \left[ -\frac{\cos 2\delta}{\lambda_D} \hat{p}_x \hat{\sigma}_x + \left( \frac{\sin 2\delta}{\lambda_D} - \frac{1}{\lambda_R} \right) \hat{p}_y \hat{\sigma}_x \right]. \quad (\text{C4})$$

Furthermore, since the  $-y$  axis is the quantized axis of a spin,  $n_z^{\text{spin}}$ , in the spin space, the Pauli matrix  $\hat{\sigma}_x$  is replaced with  $-\hat{\sigma}_y$ , and the Hamiltonian described as Eq. (A28).

#### APPENDIX D: OCCUPATION PROBABILITIES

To evaluate the occupation probabilities from spin state 1 to 8 in Fig. 2(b), we formed the following Master equations using the transition rates:

$$\frac{dP_1}{dt} = -(\Gamma_{51} + \Gamma_{81})P_1(t) + \Gamma_{15}P_5(t) + \Gamma_{18}P_8(t), \quad (\text{D1})$$

$$\frac{dP_2}{dt} = -(\Gamma_{52} + \Gamma_{82})P_2(t) + \Gamma_{25}P_5(t) + \Gamma_{28}P_8(t), \quad (\text{D2})$$

$$\frac{dP_3}{dt} = -(\Gamma_{53} + \Gamma_{63})P_3(t) + \Gamma_{35}P_5(t) + \Gamma_{36}P_6(t), \quad (\text{D3})$$

$$\frac{dP_4}{dt} = -(\Gamma_{54} + \Gamma_{74})P_4(t) + \Gamma_{45}P_5(t) + \Gamma_{47}P_7(t), \quad (\text{D4})$$

$$\begin{aligned} \frac{dP_5}{dt} = & \Gamma_{51}P_1(t) + \Gamma_{52}P_2(t) + \Gamma_{53}P_3(t) + \Gamma_{54}P_4(t) \\ & - (\Gamma_{15} + \Gamma_{25} + \Gamma_{35} + \Gamma_{45} + \Gamma_{65} + \Gamma_{75})P_5(t) \\ & + \Gamma_{56}P_6(t) + \Gamma_{57}P_7(t), \end{aligned} \quad (\text{D5})$$

$$\frac{dP_6}{dt} = \Gamma_{63}P_3(t) + \Gamma_{65}P_5(t) - (\Gamma_{36} + \Gamma_{56})P_6(t), \quad (\text{D6})$$

$$\frac{dP_7}{dt} = \Gamma_{74}P_4(t) + \Gamma_{75}P_5(t) - (\Gamma_{47} + \Gamma_{57})P_7(t), \quad (\text{D7})$$

$$\frac{dP_8}{dt} = \Gamma_{81}P_1(t) + \Gamma_{82}P_2(t) - (\Gamma_{18} + \Gamma_{28})P_8(t), \quad (\text{D8})$$

where  $P_i(t)$  ( $i = 1, \dots, 8$ ) is the occupation probability of state  $i$  in the transition diagram of Fig. 2(b). We solved these equations for a case of the steady states, i.e.,  $dP_i/dt = 0$ , and evaluated the occupation probabilities of all spin states. The transition rates are calculated by the following relations:  $\Gamma_{15} = \Gamma_{25} = \Gamma_{51} = \Gamma_{52}$ ,  $\Gamma_{35} = \Gamma_{45} = \Gamma_{53} = \Gamma_{54}$ ,  $\Gamma_{56} = \Gamma_{57}$ ,  $\Gamma_{65} = \Gamma_{75}$ ,  $\Gamma_{36} = \Gamma_{47}$ ,  $\Gamma_{63} = \Gamma_{74}$ ,  $\Gamma_{18} = \Gamma_{28} = \Gamma_{36}/2$ , and  $\Gamma_{81} = \Gamma_{82} = \Gamma_{63}/2$ .

- 
- [1] R. Scheibner, H. Buhmann, D. Reuter, M. N. Kiselev, and L. W. Molenkamp, *Phys. Rev. Lett.* **95**, 176602 (2005).
- [2] M. Josefsson, A. Svilans, A. M. Burke, E. A. Hoffmann, S. Fahlvik, C. Thelander, M. Leijnse, and H. Linke, *Nat. Nanotechnol.* **13**, 920 (2018).
- [3] G. Jalil, R. K. Puddy, R. Sánchez, A. N. Jordan, B. Sothmann, I. Farrer, J. P. Griffiths, D. A. Ritchie, and C. G. Smith, *Phys. Rev. Lett.* **123**, 117701 (2019).
- [4] B. Dutta, D. Majidi, N. W. Talarico, N. Lo Gullo, H. Courtois, and C. B. Winkelmann, *Phys. Rev. Lett.* **125**, 237701 (2020).
- [5] R. Sánchez and M. Büttiker, *Phys. Rev. B* **83**, 085428 (2011).
- [6] A. N. Jordan, B. Sothmann, R. Sánchez, and M. Büttiker, *Phys. Rev. B* **87**, 075312 (2013).
- [7] P. Strasberg, G. Schaller, T. L. Schmidt, and M. Esposito, *Phys. Rev. B* **97**, 205405 (2018).
- [8] R. Sánchez, P. Samuelsson, and P. P. Potts, *Phys. Rev. Res.* **1**, 033066 (2019).
- [9] Y. Zhang and Z. Xie, *Phys. Rev. E* **104**, 064142 (2021).
- [10] S. Kamimura, H. Hakoshima, Y. Matsuzaki, K. Yoshida, and Y. Tokura, *Phys. Rev. Lett.* **128**, 180602 (2022).
- [11] T. Yamamoto, Y. Tokura, and T. Kato, *Phys. Rev. B* **106**, 205419 (2022).
- [12] K. Kuroyama, S. Matsuo, J. Muramoto, S. Yabunaka, S. R. Valentin, A. Ludwig, A. D. Wieck, Y. Tokura, and S. Tarucha, *Phys. Rev. Lett.* **129**, 095901 (2022).
- [13] T. Fujisawa, D. G. Austing, Y. Tokura, Y. Hirayama, and S. Tarucha, *Nature (London)* **419**, 278 (2002).
- [14] R. Hanson, L. H. Willems van Beveren, I. T. Vink, J. M. Elzerman, W. J. M. Naber, F. H. L. Koppens, L. P. Kouwenhoven, and L. M. K. Vandersypen, *Phys. Rev. Lett.* **94**, 196802 (2005).
- [15] T. Meunier, I. T. Vink, L. H. Willems van Beveren, K.-J. Tielrooij, R. Hanson, F. H. L. Koppens, H. P. Tranitz, W. Wegscheider, L. P. Kouwenhoven, and L. M. K. Vandersypen, *Phys. Rev. Lett.* **98**, 126601 (2007).
- [16] V. N. Golovach, A. Khaetskii, and D. Loss, *Phys. Rev. Lett.* **93**, 016601 (2004).
- [17] J. Danon, *Phys. Rev. B* **88**, 075306 (2013).
- [18] N. Hartman, C. Olsen, S. Lüscher, M. Samani, S. Fallahi, G. C. Gardner, M. Manfra, and J. Folk, *Nat. Phys.* **14**, 1083 (2018).
- [19] K. Ono, S. N. Shevchenko, T. Mori, S. Moriyama, and F. Nori, *Phys. Rev. Lett.* **125**, 166802 (2020).
- [20] R. Hanson, L. P. Kouwenhoven, J. R. Petta, S. Tarucha, and L. M. K. Vandersypen, *Rev. Mod. Phys.* **79**, 1217 (2007).
- [21] V. F. Maisi, A. Hofmann, M. Rösli, J. Basset, C. Reichl, W. Wegscheider, T. Ihn, and K. Ensslin, *Phys. Rev. Lett.* **116**, 136803 (2016).
- [22] T. Fujita, P. Stano, G. Allison, K. Morimoto, Y. Sato, M. Larsson, J.-H. Park, A. Ludwig, A. D. Wieck, A. Oiwa, and S. Tarucha, *Phys. Rev. Lett.* **117**, 206802 (2016).
- [23] A. Hofmann, V. F. Maisi, T. Krähenmann, C. Reichl, W. Wegscheider, K. Ensslin, and T. Ihn, *Phys. Rev. Lett.* **119**, 176807 (2017).
- [24] A. Hofmann, C. Karlewski, A. Heimes, C. Reichl, W. Wegscheider, G. Schön, K. Ensslin, T. Ihn, and V. F. Maisi, *Phys. Rev. Res.* **2**, 033230 (2020).
- [25] H. Grabert and M. H. Devoret, *Single Charge Tunneling: Coulomb Blockade Phenomena in Nanostructures*, 1st ed., NATO ASI Series B: Physics Vol. 294 (Springer Science Business Media, LLC, New York, 1992).
- [26] R. Aguado and L. P. Kouwenhoven, *Phys. Rev. Lett.* **84**, 1986 (2000).
- [27] S. Matsuo, K. Kuroyama, S. Yabunaka, S. R. Valentin, A. Ludwig, A. D. Wieck, and S. Tarucha, *Phys. Rev. Res.* **2**, 033120 (2020).

- [28] S. Sasaki, T. Fujisawa, T. Hayashi, and Y. Hirayama, *Phys. Rev. Lett.* **95**, 056803 (2005).
- [29] Z. White and G. Ramon, *Phys. Rev. B* **97**, 045306 (2018).
- [30] F. H. L. Koppens, J. A. Folk, J. M. Elzerman, R. Hanson, L. H. W. van Beveren, I. T. Vink, H. P. Tranitz, W. Wegscheider, L. P. Kouwenhoven, and L. M. K. Vandersypen, *Science* **309**, 1346 (2005).
- [31] V. Fock, *Z. Phys.* **47**, 446 (1928).
- [32] C. G. Darwin, *Math. Proc. Cambridge Philos. Soc.* **27**, 86 (1931).
- [33] E. Barnes, J. P. Kestner, N. T. T. Nguyen, and S. Das Sarma, *Phys. Rev. B* **84**, 235309 (2011).
- [34] E. Nielsen, E. Barnes, J. P. Kestner, and S. Das Sarma, *Phys. Rev. B* **88**, 195131 (2013).
- [35] V. N. Golovach, A. Khaetskii, and D. Loss, *Phys. Rev. B* **77**, 045328 (2008).
- [36] R. Hanson, L. M. K. Vandersypen, L. H. W. van Beveren, J. M. Elzerman, I. T. Vink, and L. P. Kouwenhoven, *Phys. Rev. B* **70**, 241304(R) (2004).